Spring 2014

Fluid-Structure Interaction Modeling of A F/A-18 Twin-Tail Buffet Using Non-linear Eddy Viscosity Models

Ahmed M. Nagib M. Elmekawy
Old Dominion University

FLUID-STRUCTURE INTERACTION MODELING OF A F/A-18 TWIN-TAIL BUFFET USING NON-LINEAR EDDY VISCOSITY MODELS

by

Ahmed M Nagib M. Elmekawy
B.S. June 2006, Alexandria University, Egypt
M.S. August 2009, Alexandria University, Egypt

A Dissertation Submitted to the Faculty of
Old Dominion University in Partial Fulfillment of the
Requirements for the Degree of

DOCTOR OF PHILOSOPHY

AEROSPACE ENGINEERING

OLD DOMINION UNIVERSITY
May 2014

Approved by:

Oktay Baysal (Director)

Duc Nguyen (Member)

Onur Bilgen (Member)

ABSTRACT

FLUID-STRUCTURE INTERACTION MODELING OF A F/A-18 TWIN-TAIL BUFFET USING NON-LINEAR EDDY VISCOSITY MODELS

Ahmed M Nagib M. Elmekawy
Old Dominion University, May 2014
Director. Dr. Oktay Baysal

When turbulent flow generates unsteady differential pressure over an aircraft's structure, this may generate buffeting, a random oscillation of the structure. The buffet phenomenon is observed on a wide range of fighter aircraft, especially fighters with twin-tail. More research is needed to better understand the physics behind the vortical flow over a delta wing and the subsequent tail buffet.

This dissertation reports the modeling and simulation of a steady-state one-way fluid-structure interaction for the tail buffet problem observed on a F/A-18 fighter. The time-averaged computational results are compared to available experimental data. Next, computations are extended to simulate an unsteady two-way fluid-structure interaction problem of the tail buffet of a F/A-18 fighter.

For the modeling herein, a commercial software ANSYS version 14.0, is employed. For the fluid domain, the unsteady Reynolds-averaged Navier Stokes (URANS) equations with different turbulent models are utilized. The first turbulence model selected is the modified Spalart-Allmaras model (SARRC) with a strain-vorticity based production and curvature treatment. The second turbulence model selected is the Non-linear Eddy Viscosity Model (NLEVM) based on the Wilcox k–ω model. This model uses the formulation of an explicit algebraic Reynolds stress model. The structural

simulation is conducted by a finite element analysis model with shell elements. Both SARRC and NLEVM turbulence models are in ANSYS software.

The experimental data used for validation were conducted on a simplified geometry: a 0.3 Mach number flow past a 76-deg delta wing pitched to 30-deg. Two vertical tails were placed downstream of the delta wing.

The present work is the first ever study of the tail buffet problem of the F/A-18 fighter with two-way fluid-structure interaction using the two advanced turbulence models. The steady-state, time-averaged, one-way fluid-structure interaction case of the present investigation indicates that simulations employing the NLEVM and SARRC turbulence models do not match the experimental data. These results are somewhat expected for the steady-state, one-way simulation, because it involves no force and displacement transfer between the fluid and structural domains.

For the unsteady two-way fluid-structure interaction case, both models result in more favorable agreement with the experimental data by optimizing the available computational resources particularly when compared to prior simulations by other researchers. Results from the NLEVM model produce improved pressure predictions on the tail as compared to the results from the SARRC model.

Based on the simulation results, it is concluded that the buffet problem should be simulated as a two-way fluid-structure interaction. The NLEVM turbulence model is recommended in predicting vortical flow characteristics over a delta wing. The NLEVM turbulence model is necessary to predict the pressure distribution not only over the aircraft surface but also the tails since they experience the wake of vortices.

This dissertation is dedicated, with love, to my parents, my wife and my daughter.

ACKNOWLEDGEMENTS

First, I would like to express my sincere and heartfelt thanks to my original advisor Professor Osama Kandil. I considered myself lucky to work with him and I learned a lot from him. He showed continuous patience, encouragement and support throughout my journey as a graduate student.

I owe a debt of gratitude to Professor Oktay Baysal for accepting to be my advisor in the latter stages of my dissertation. The completion of this dissertation would have been impossible without his guidance and encouragement.

I wish to express my special thanks to Professor Keejoo Lee for his help, support and for his suggestions in the early stages of this dissertation.

I am extremely thankful to Dr. Onur Bilgen and Professor Duc Nguyen for being a part of my committee and reviewing the manuscript. Also, I owe special thanks to Professor Ali Beskok for reviewing the early version of the manuscript.

The financial support of the Mechanical and Aerospace Engineering Department of Old Dominion University is gratefully acknowledged.

Finally, I want to express a special debt of gratitude to my parents Mr. Mohamed Nagib, Mrs. Mervat Ebieda and my wife Mrs. Samar Badr Eldin. Without their unconditional love, I could have never come so far. This dissertation is dedicated to them.

NOMENCLATURE

Symbols

a_{ij}	Anisotropic Component of Reynolds stress tensor
$a_{ij}^{(ex)}$	Extra anisotropic component of Reynolds Stress tensor for NLEVM model
c_{b1}, c_{b2}	Model constants for Spalart-Allmaras turbulence model
c_{r1}, c_{r2}, c_{r3}	Model constants for SARC turbulence model
c_{w1}	Model constant for Spalart-Allmaras turbulence model
d	Distance from wall
e	Specific internal energy
f_i	Body forces
f_{r1}	Rotation function for SARC turbulence model
f_{v1}, f_{v2}, f_w	Model functions for Spalart-Allmaras turbulence model
k	Turbulent kinetic energy
k_T	Heat Transfer coefficient
p	Pressure
q_i	Heat flux vector
t	Time
u_i	Instantaneous velocity vector
$\bar{u}_i$	Time averaged velocity vector
u_i'	Turbulent fluctuating velocity
x_i	Position vector
x, y, z	Cartesian coordinates
C_μ^{eff}	Effective eddy viscosity coefficient for NLEVM model
C_τ	Model constant for NLEVM model
C_{prod}	Model constant for SAR turbulence model
C_{v1}	Model constant for Spalart-Allmaras turbulence model
$D, \widetilde{D}$	Model constants for SARC turbulence model
E	Total energy

I	Identity matrix
II_Ω, IV	Invariants of strain-rate and rotation tensors
M	Mach number
P	Pressure
P_ω	Production term in ω equation
P_k	Production term in k equation
R	Specific gas constant
Re	Reynolds number
S	Magnitude of vorticity; Magnitude of strain-rate tensor
S_{ij}	Strain-rate tensor
$\bar{S}_{ij}$	Mean strain-rate tensor
T	Temperature
U_i	Mean flow velocity vector
[M]	Structural mass matrix
[C]	Structural damping matrix
[K]	Structural stiffness matrix
$\{\ddot{U}\}$	Nodal acceleration vector
$\{\dot{U}\}$	Nodal velocity vector
{U}	Nodal displacement vector
[F]	Applied load vector due to Aerodynamic Loads

Greek Symbols

α	Angle of incidence (attack)
α	Model constant for $k-\omega$ model
β_n	Model coefficient for NLEVM model
β^*	Closure coefficient for $k-\omega$ model
δ_{ij}	Kronecker delta, $\delta_{ij} = 1\ if\ i = j\ and\ \delta_{ij} = 0\ if\ i \neq j$
$\varepsilon_{i,j,k}$	Alternating symbol
μ	Molecular viscosity

μ_T	Turbulent eddy viscosity
ν	Kinematic viscosity, $\nu = \mu/\rho$
$\tilde{\nu}$	Spalart-Allmaras equation working variable
ρ	Density
$\bar{\rho}$	Time-averaged density
σ^*	$k-\omega$ model constant
τ_{ij}	Viscous stress tensor
τ_{ij}^R	Reynolds stress tensor
χ	Model function for Spalart-Allmaras model
ω	Dissipation per unit turbulence kinetic energy
ω_i	Vorticity vector
Ω	Magnitude of rotation sensor
Ω_{ij}	Rotation Tensor
$\overline{\Omega}_{ij}$	Mean rotation tensor
Ω_m^{Rot}	Rotation Tensor with respect to the reference frame

Acronyms

ANSYS Fluent	Used fluid solver
ANSYS Mechanical	Used structural solver
CFD	Computational Fluid Dynamics
LES	Large Eddy Simulations
LEX	Leading edge extension
DES	Detached Eddy Simulation
DNS	Direct Numerical Simulation
NASA	National Aeronautics and Space Agency
NLEVM	Non-Linear Eddy Viscosity Model
RANS	Reynolds Averaged Navier Stokes
RMS	Root Mean Square
SA	Spalart-Allmaras

SAR	Spalart-Allmaras with Rotation Correction
SARC	Spalart-Allmaras with Rotation/Curvature Correction
SARRC	Spalart-Allmaras with Rotation and Rotation/Curvature Corrections
SOLID186	Type of the shell element used in the structural solver
URANS	Unsteady Reynolds Averaged Navier Stokes

TABLE OF CONTENTS

Page

LIST OF TABLES

LIST OF FIGURES

CHAPTER 1

INTRODUCTION AND LITERATURE REVIEW

1.1 Introduction

In this chapter, the literature review of previous experimental and numerical investigations for the tail buffet problem induced by vortical flow over a delta wing is presented. The motivation and objectives of this dissertation are presented.

1.1.1 The Buffet Problem

The airframes of modern high speed aircraft have suffered from aeroelastic tail buffeting problems for decades [1]. This tail buffeting is stimulated by the differential pressure caused by the unsteady turbulent flow over delta wing fighters. The tail buffeting may lead to failure of structural components of modern high speed aircraft and reduces mission availability and performance. Tail buffet increases the cost of inspection, repair and replacements [2]. Moreover, restrictions on the angle of attack and speed at which a certain maneuvers can be flown are forced and limited during missions as shown in Figures 1.1 and 1.2 [3]. This aeroelastic phenomenon still remains one of the most challenging problems in aerospace design. A better modeling of the turbulent flow is required for current and future modern high performance aircraft.

The first recorded tail buffet problem was the loss of a small transport airplane in England in 1930 [4]. Buffet problems affect a wide range of fighters, but it plagues the twin-tail fighter aircraft particularly [5]. Since twin-tail configuration are selected for 5^{th} generation fighters such as the American F-35 and the Russian Sukhoi PAK FA (T-50), as shown in Figures 1.3, 1.4 and 1.5, more research and experimental data should be

conducted for a better understanding of the physics of vortical flow over delta wing and the corresponding tail buffet.

Figure 1.1.Vortices from the leading edge of a twin-tail fighter aircraft, generated at high angle of attack, breakdown upstream of the vertical tail [6].

Figure 1.2.Vortices breakdown upstream of the vertical tail [7].

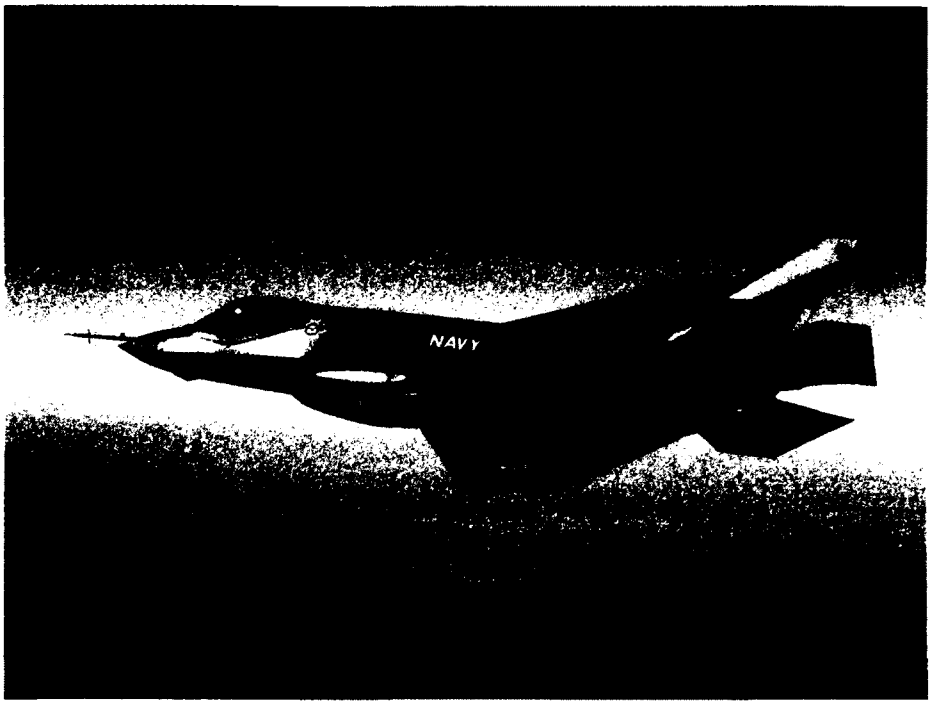

Figure 1.3. The American F-35 [8].

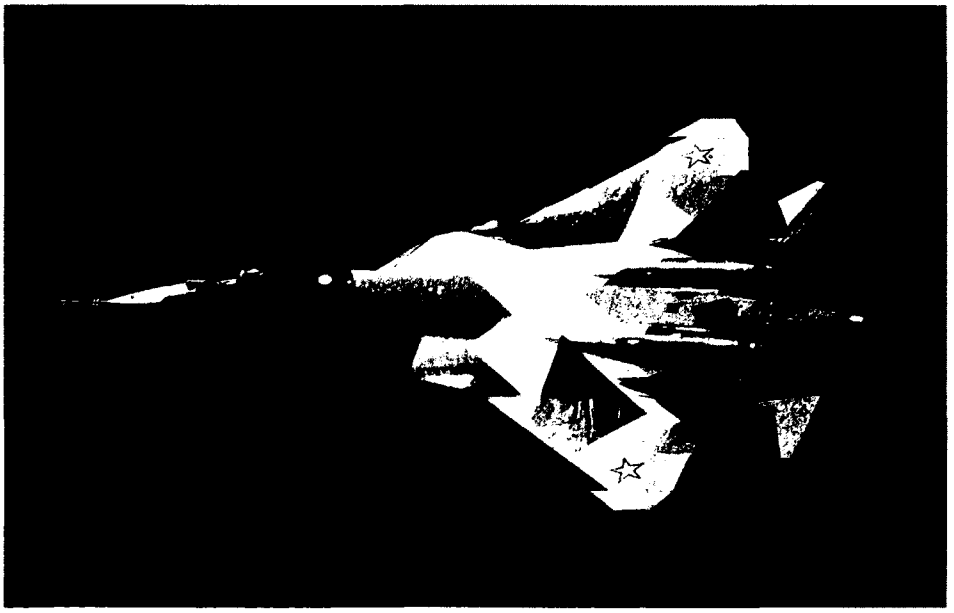

Figure 1.4. The Russian Sukhoi PAK FA (T-50) [9].

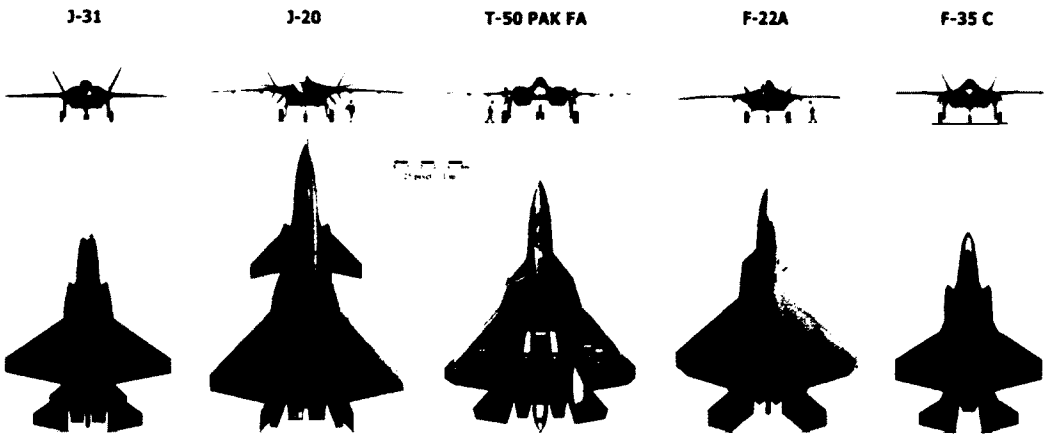

Figure 1.5. Examples of the 5th generation fighters [10].

The first discovery of a tail buffet problem for modern fighter aircraft was the F-15 manufactured by McDonnell Douglas. Fatigue cracks were discovered, and subsequent investigations showed that tail buffet was the reason [5]. Maintenance and replacement of F-15 vertical tails due to cyclic load damage was five to six million dollars per year in 1998. There are other fighter aircrafts with twin-tail such as the F/A-18 and the F/A-22, which suffer from buffet problem [3].

The buffet problem also occurs in single tail fighters such as the F-16 manufactured by General Dynamics, which suffers ventral fin damage due to buffet. Early in the 1980s, when the Low Altitude Navigation and Targeting Infrared for Night (*LANIRN*) pods were installed, ventral fin failure was observed. Figure 1.6 shows the ventral fin failure following the first F-16 flight with *LANTIRN* pods [2]. Previous flight trials and wind tunnel tests have shown that a significant portion of the fatigue damage on the vertical fin was caused by stresses resulting from the first bending and first torsion vibration modes of the vertical fin. The frequency content and the intensity of the fin buffet load vary primarily as a function of angle of attack and the dynamic pressure [11].

The F/A-18 A/B buffet problem was first observed early in service deployments when cracks were found on the root stub structure. A special inspection on the tails of F/A-18 is recommended every 200 flight hours due to fatigue problems that lead to safety problems and high maintenance costs [12]. Lee *et al.* [13], Lee and Valerio [14] and Thompson [15] showed that the pressure fluctuations formed by the breakdown of vortices over the upper surface of the F/A-18 delta wing are the cause of the tail buffet at high angle of attacks. The dominant frequency of this pressure fluctuation was near the natural frequency of the primary mode of the tails; therefore, the tails vibrated with larger amplitude than expected.

Figure 1.6. Ventral fin failure of F/16 following its first flight with *LANTIRN* [2].

The F/A-18 was selected for the present research because it was the test bed for many research organizations such as NASA [13], Technical Cooperation Program (TTCP), which consists of the defense departments of five nations (Australia, Canada, New Zealand, United Kingdom, and the United States), and the International Follow On Structural Test Program (IFOSTP) by Canada and Australia [15 and 16]. The F/A-18 was selected by these organizations because it gives a good example of the leading edge extension vortical flow generated by future generations of fighter aircraft.

1.1.2 Vortical Flow over Delta Wing

A better understanding and explanation of the physics of vortical flows around an aircraft has challenged aerodynamicists for decades. Non-linear vortex lift was identified since the concept of swept aircraft wings was introduced. The sweeping of an aircraft wing delays the onset of compressibility effects and achieves better performance at high angle of attacks [17].

A comparison between the non-linear vortex lift to the total lift of a slender sharp delta wing is shown in Figure 1.7. As described by Hoeijmakers [18], these vortical structures are commonly formed by shear layer separation which begins at the leading edge of highly swept wings at high angle of attack. The shear layer rolls up starting from the leading edge and develops a stable vortex. This vortex generates high velocity and low pressure on the upper surface of the delta wing which leads to additional lift forces. The vortical flow features over a delta wing are shown in Figures 1.8 and 1.9. Polhamus [19] published a comprehensive review of the evolution of the slender wing in vortex lift research.

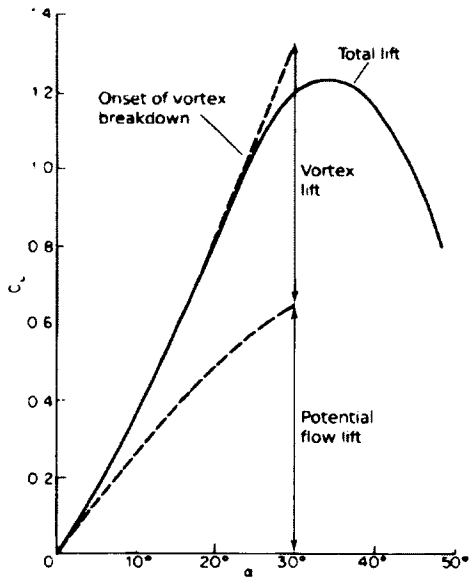

Figure 1.7. Non-linear contribution of vortex lift to total lift [17].

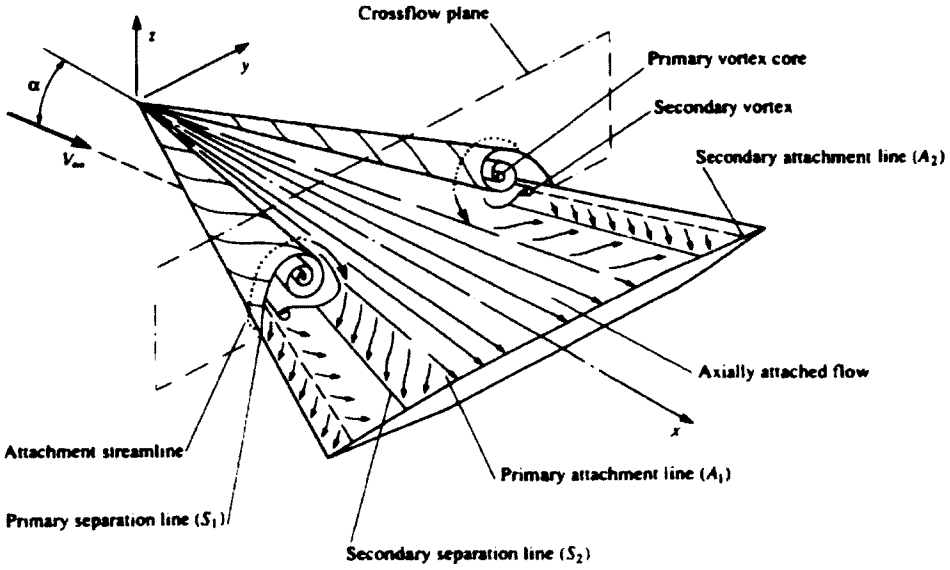

Figure 1.8. View of leading-edge (primary) vortex and secondary vortex with upper-side surface flow directions [20].

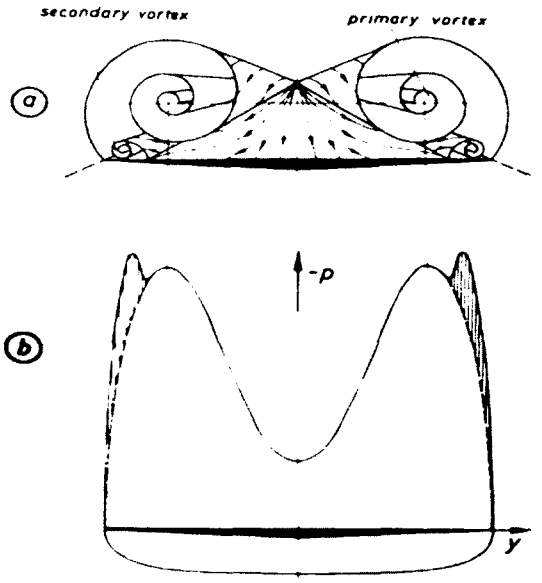

Figure 1.9. Sharp edged slender wing vortex flow [21].

1.2 Previous Experimental Investigations

Various experiments have been performed on the F/A-18 aircraft, including small-scale wind and water tunnels, full scale wind tunnel and flight tests [1]. Some of the important sub-scale and full-scale test results will be briefly discussed in this section.

1.2.1 Sub-scale Experimental Tests

Sellers [22], Erickson [23] and Wentz [24] performed experimental investigations on a sub-scale model of the F/A-18 and observed that at angles of attack of 25-deg and higher, the breakdown of leading edge extension vortices occurred downstream of the vertical tails. Based on the experimental data of a 6% scale model of the F/A-18, Erickson [23] found that the leading edge extension vortices are dominant when compared with the weak forebody vortices at all Mach numbers.

Figure 1.10 shows a typical dye picture of a 1/72 scale model at a Reynolds number of 500 and angle of attack of 30-deg taken by Lee [25], showing the vortex core

transition from tight shape to the breakdown point where a sudden expansion occurs. Lee observed asymmetry between the left and right vortex breakdown positions with a scatter of typically 5 - 10%. Moreover, it was found that by increasing the angle of attack the breakdown point moves upstream.

The experimental data used in the numerical simulation in this dissertation were published by Washburn *et al.* [26]. A simplified geometry of a rectangular plate and subsonic flow at a Mach number 0.3 over a 76-deg delta wing at angle of attack of 30-deg was employed. Two vertical tails were placed downstream of the delta wing. Although Washburn used a simplified model to isolate the primary flow feature of concern (the leading edge extension vortices), his result showed similarities between the buffet flow characteristics of the simplified geometry and the F/A-18 flight test data.

A rigid 16% full-span model of the F/A-18 aircraft was tested by Moss *et al.* [27] for a range of Mach numbers from 0.3 to 0.5 and angle of attack range from 10 to 40-deg. The results showed that the largest response due to pressure fluctuation occurred in the first bending mode and the largest buffet response happened at a Mach number 0.3 when compared to other Mach numbers. It was observed that the response increased as the dynamic pressure was increased.

Based on the findings of Moss [27], Sellers [22] and Washburn [26], the numerical simulation in the present dissertation will be conducted for a simplified geometry of 76-deg swept, rectangular plate at a Mach number 0.3 and at an angle of attack of 30-deg. This configuration was selected to get the breakdown position of the vortices upstream of the vertical tail, as the largest buffet response occurs at these particular set of parameters.

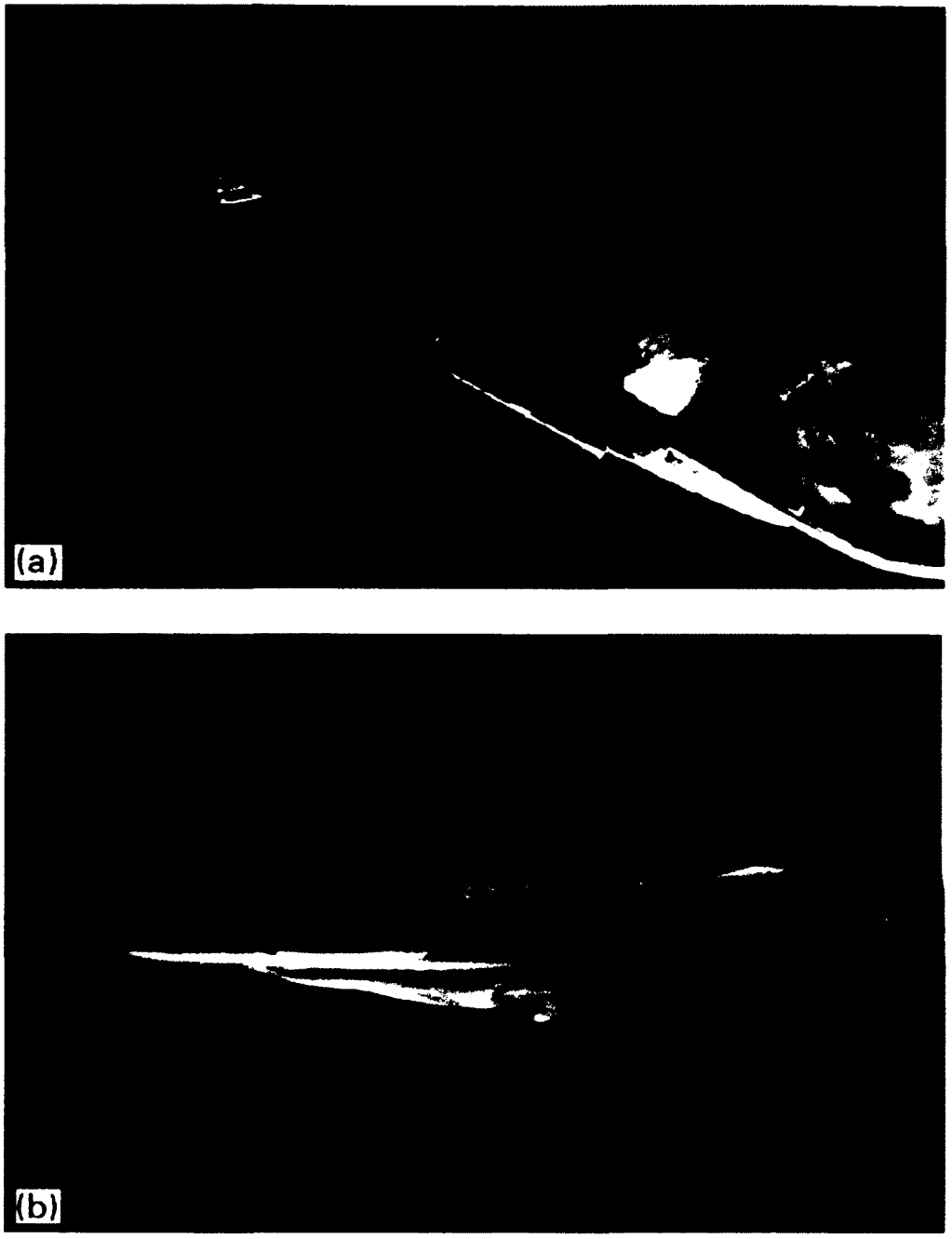

Figure 1.10. (a) Side view, (b) plan view of the CF-18 aircraft model and vortex at angle of attack of 30-deg [25].

1.2.2 Full-scale Experimental Tests

In the full scale 80 ft x 120 ft wind tunnel of the National Full-Scale Aerodynamic Complex, the NASA Ames Research Center performed full scale buffet tests over the range of angles of attack from 18 to 50-deg. The side slip angle varied from 0.15 to 15-deg to provide a comparison between full-scale data and sub-scale wind tunnel model data [28, 29, 30, and 31].

A comparison between flight test, full-scale wind tunnel data and the sub-scale wind tunnel data for the F/A-18 was published by Meyn *et al.* [32]. Another comparison between the full scale tail buffet data at NASA Ames and the 16%-scale model was conducted by Moses and Pendleton [33]. Both Meyn *et al.*, Moses and Pendleton showed that the sub-scale tests are adequate for estimating the characteristics of the differential pressure on the tail.

Figure 1.11 shows a typical flow visualization of the leading edge extension (LEX) vortex of the F/A-18 at side slip angle of -1.4-deg and angle of attack of 25-deg. The picture captured by Fisher [34] shows the path and the breakdown of the vortex.

1.3 Previous Numerical Investigations

1.3.1 Tail Buffeting Simulations

The first computational simulation of the tail buffet problem was conducted by Kandil *et al.* [35]. A 76-deg swept delta wing and a single tail configuration were utilized. The flow was modeled by laminar, unsteady and compressible Navier-Stokes equations. The tail was modeled as a beam. No comparison between the simulation and experimental data was reported.

Figure 1.11. Flow visualization of LEX vortex core of the F/A-18 at angle of attack of 25-deg and side slip angle of -1.4-deg [34].

Kandil, Sheta and Massey [36] studied the tail buffet problem by using a 76-deg delta wing and twin-tail configuration. The flow was modeled by unsteady, compressible, full Navier-Stokes equations. Only uncoupled bending-torsion response was studied. The simulation results were not validated with experimental data.

Sheta [37] and Massey [38] studied the tail buffet problem by using a 76-deg delta wing and twin-tail configuration. Rigid and flexible tail configurations at different Mach numbers were simulated. The flow was modeled by unsteady, compressible, full Navier-Stokes equations. Coupled bending-torsion response of the tail was studied. The simulation results were validated with experimental data.

Findaly [39] simulated the buffet response of a rigid and flexible tail configurations and delta wing by using coupled dynamic aeroelastic analysis. The results

showed under-prediction of the buffet pressure and showed that the rigid tail computations over predicted the flight data.

Leviniski [1] studied the buffet response of a rigid and flexible tail configurations and delta wing by using aeroelastic model. Unsteady vortex model was used for the fluid domain. Coupled aeroelastic equations for the bending and torsional deflections of the tail were used for the structural domain. The results showed under-prediction of the buffet pressure and showed that the rigid tail computations over predicted the flight data.

Sheta 2003 [40] employed the fluid dynamics module CFD-FASTRAN and three-dimensional direct finite element analysis to simulate the buffet response of a full scale F-A/18. The alleviation of the tail buffet by using LEX fens was studied. The results showed under-prediction of the buffet pressure.

Guillaume *et al.* 2010 [41] employed the Navier-Stokes Multi Block (NSMB) CFD code and unsteady aeroelastic coupling algorithm to simulate the buffet pressure of a full F/A-18 model. DES algorithm with Spalart-Allmares and $k-\omega$ Menter Shear Stress turbulence models were used. The results showed a 30% deviation of the RMS pressure coefficient of the numerical data and flight test data at angle of attack of 30-deg.

Table 1.1 lists the average error between the computed RMS pressure values by different researchers and the experimental data. All the researchers listed in Table 1.1 conducted two-way fluid-structure interaction simulations of the tail buffet of F/A-18 but used linear eddy viscosity model turbulence models. In this dissertation, non-linear eddy viscosity turbulence models will be used to simulate the tail buffet of F/A-18 fighter.

In Chapter 3, the computed RMS non-dimensional pressure distribution of the inner and outer surfaces of the tail will be computed and compared with the experimental data by Washburn [26].

Table 1.1. Comparison of the numerically computed RMS non-dimensional pressure distribution on the tail surface by different researchers.

Researcher	Average error between the computed RMS pressure values and Experimental data	F/A-18 model
Massey [38]	63%	Simplified Geometry
Leviniski [1]	40%	Simplified Geometry
Sheta [40]	37%	Full-scale
Guillaume [41]	32%	Full-scale

1.3.2 Computational Fluid Dynamics Simulations of Delta Wing Vortical Flows

The choice of the turbulence model to use for the CFD rendering of the vortex flow is critical to the success of understanding and controlling the buffet [42]. The current approaches, in increasing complexity, range from inviscid, laminar, Unsteady Reynolds Averaged Navier-Stokes (URANS), Detached Eddy Simulation (DES), Large Eddy Simulation (LES) to the Direct Numerical Simulation (DNS) method. The trade-off between computational resources and the solution fidelity, when compared to experimental data, affects the choice of the turbulence model. Below is a comparison between the turbulence models and their capability to model the vortical flow:

1. Euler simulation, although it is capable of capturing and predicting the vortical interaction and breakdown, is not capable of predicting secondary separation.
2. Unsteady Reynolds Averaged Navier-Stokes (URANS) can predict the secondary separation successfully. However, it predicts a higher level of the turbulence in the vortex core, which leads to a failure in predicting the vortex breakdown. Some

treatments to the turbulence models [43] can limit the production term in the strain tensor in vortex core. The computation cost is higher than Euler, but much less than DES, LES and DNS.

3. Detached Eddy Simulation (DES) [44] has been used to solve the problem of predicting high level of turbulence in the vortex core by using Large Eddy Simulation (LES). DES is implanted by using URANS model at boundary layer near the wall where LES computational cost would be high at a typical flight Reynolds numbers and using LES away from walls. Although some promising results were published by using DES, the simulation is more costly than URANS in terms of finer grid and smaller time step that are required.
4. Finally, Large Eddy Simulation (LES) and Direct Numerical Simulation (DNS) [45] can be used and give a better result from the previous methods but at the expense of the required computational resources especially at flight Reynolds numbers due to the required grid refinement and small time step.

The URANS method will be used in this dissertation. This method can capture the flow characteristics efficiently and it is relatively inexpensive when compared to DES, LES and DNS.

1.3.2.1 Turbulence Modeling for Unsteady Reynolds Averaged Navier-Stokes (URANS) Method

To determine the suitable turbulence model for vortical flow which gives better results compared to experimental data, more research should be conducted [46]. The following are some examples demonstrating this necessity.

Grodnier [47] used the standard linear $k-\omega$ turbulence model to predict the flow over a 65-deg delta wing and a Mach number 0.37. It was concluded that the linear $k-\omega$ turbulence model predicted an excessive amount of eddy viscosity in the vortex core which lead to weaker vortices, and it was recommended not to use the linear $k-\omega$ turbulence model for this type of flow.

To solve the problem of the higher eddy viscosity around the primary vortex core, some modifications to the linear $k-\omega$ turbulence model were proposed based on limiting the production of the turbulent kinetic energy, P_k, in the vortex core region by taking the rotation of the vortex into account. Another modification enhanced the production of the dissipation rate, P_w, to reduce the eddy viscosity in the vortex core. These two modifications were not used in the simulations conducted in this dissertation.

Brandsma *et al.* [43] investigated the effect of the previous two modifications to the linear $k-\omega$ turbulence model on a 65-deg cropped delta wing at a Mach number 0.8 and an angle of attack of 10-deg. It was concluded that the modification which utilized the enhancement of the production of the dissipation rate, P_w, gave a better result when compared to the experimental data and should be used for future simulation of the vortical flow compared to the modification which limited the production of the turbulent kinetic energy, P_k. The modification, which limited the production of the turbulent kinetic energy, P_k, was found to be more diffusive than the production of the dissipation rate, P_w, enhancement modification and was not able to reduce the turbulence in the vortex core adequately.

Wallin, Johansson [48], and Hellsten [49] proposed a modification to the standard linear Wilcox $k-\omega$ turbulence model [50, 51] for vortical flows by using a non-linear

eddy viscosity model (NLEVM). This NLEVM is based on an explicit algebraic Reynolds stress model by adding an extra anisotropic Reynolds stress term to Boussinesq's approximation. An increase of the dependence of the NLEVM model behavior on the mean rotation tensor has been achieved. More details can be found in [52, 53 and 54]. The NLEVM turbulence model will be used in this dissertation.

Dol *et al.* [55] compared NLEVM and the two modifications used by Brandsma [43] by studying the flow over a 65-deg cropped delta wing. Dol concluded that the NLEVM and the two rotation correction turbulence models give better results when compared to the standard $k-\omega$ model. The two rotation correction models over predicted the suction peak on the surface of the wing. Moreover, the NLEVM showed a better agreement with the experimental data. Dol recommended the NLEVM for capturing the vortical flow over delta wings.

Soemarwoto and Boelens [56] studied the effect of NLEVM over delta wing flow and concluded that using NLEVM yielded improvement in moment coefficient and pressure at the wing tip region.

Schiavetta *et al.* [57] studied the flow over a delta wing and compared NLEVM and SA turbulence models and DES. Schiavetta concluded that the NLEVM turbulence model could capture the flow characteristics with acceptable accuracy when compared to DES results for the same grid. Schiavetta also indicated that NLEVM is adequate to model the behavior for the purpose of predicting buffet response because it captures the main frequencies of the flow.

To solve the problem of the higher eddy viscosity around the primary vortex core, some modifications to the Spalart-Allmaras turbulence model [58] were proposed by

Mariani *et al.* [59 and 60], Spalart and Shur [61] and Shur *et al.* [62]. These modifications are based on reducing the turbulent eddy viscosity in high rotational flows. These modifications will be used in this dissertation by using Spalart-Allmaras turbulence model with Rotation and Rotation/Curvature Corrections (SARRC).

Morton *et al.* [63 and 64] studied the vortical flow over a 70-deg semi-span delta wing and compared Spalart-Allmaras (SA), Spalart-Allmaras with a Rotation Correction (SARC), Menter's Shear Stress Transport model (SST), and DES computations with the experimental data. Morten indicated that SA and SST turbulence models are unable to resolve the majority of the frequency content of the steady-state results. Although SARC showed an improved spectrum before breakdown, it did not capture the mid to high frequencies after the breakdown. Moreover, DES showed more accurate results of the vortex breakdown behavior.

1.4 Motivation

As observed from the literature survey, many simulations have been conducted by using linear eddy viscosity models on the two-way fluid-structure interaction of the tail buffet of the F/A-18 fighter. Previous simulation results, however, overpredict the pressure on the tails. The URANS method is relatively inexpensive and does not require as finer a grid or as smaller a time step as compared to DES, LES and DNS, yet it is capable of predicting the buffet response. It captures the main frequencies of the flow oscillations. The two non-linear eddy viscosity turbulence models, NLEVM and SARRC, may be the way to capture the buffet problem of the flow over delta wing, since they depend more on both rotation and strain-rate. Both SARRC and NLEVM turbulence models are in ANSYS software. NLEVM and SARRC turbulence models should add

more fidelity to the simulation when compared to experimental data. The present work is the first ever study of tail buffet problem of the F-A/18 fighter with two-way fluid-structure interaction and using the two advanced non-linear eddy viscosity turbulence models: NLEVM and SARRC.

1.5 Objectives

As a baseline, the simulations will be conducted for the one-way fluid-structure interaction simulations by incorporating the SARRC and NLEVM turbulence models. Then, the two-way fluid-structure interaction simulations will be performed, again using SARRC and NLEVM turbulence models. A comparison between the RMS values of the pressure on the tail at five different locations will be conducted. The hypothesis is such that, this never before tried approach, a two-way fluid-structure interaction coupled with non-linear eddy viscosity turbulence models, should produce closer results of the differential pressure on tail surfaces when compared to the available experimental data, within the optimized available computational resources. This differential pressure forces the tails to oscillate that is known as buffet.

1.6 Dissertation Outline

In this dissertation, Chapter 2 of presents the governing equations for structural and CFD simulations, turbulence models, mesh details and experimental data used in the investigations. Chapter 3 presents the results and discussion of the numerical simulations to show the ability of the turbulence models to predict the unsteady behavior of the subsonic flow and the pressure affecting on the tail surface. Finally, Chapter 4 reports overall conclusions and recommendations for future research.

CHAPTER 2

METHODOLOGY OF COMPUTATIONAL FLUID DYNAMICS & COMPUTATIONAL STRUCTURAL DYNAMICS INVESTIGATIONS

2.1 Introduction

In this chapter, the governing equations for both fluid and structural models are presented. The primary references for the governing equations are given by [65, 50 and 46]. The commercial ANSYS software is used in this dissertation to perform the simulations. The element and grid selection in ANSYS are presented. In addition, the validated experimental data by Washburn [26] will be presented.

2.2 The Navier-Stokes Equations

The Navier-Stokes Equations are a set of Partial Differential Equations (PDEs) which describe the conservation laws for mass, momentum and energy, given by,

• Mass, the continuity equation,

$$\frac{\partial \rho}{\partial t} + \frac{\partial (\rho u_i)}{\partial x_i} = 0 \tag{2.1}$$

• Momentum

$$\frac{\partial \rho u_i}{\partial t} + \frac{\partial (\rho u_i u_j)}{\partial x_j} = -\frac{\partial P}{\partial x_i} + \frac{\partial \tau_{ij}}{\partial x_j} \tag{2.2}$$

where τ_{ij} is s the viscous stress tensor, and is proportional to the strain-rate tensor for a Newtonian fluid, and is given by,

$$\tau_{ij} = 2\mu S_{ij} \tag{2.3}$$

where the viscous strain-rate tensor S_{ij} is given by,

$$S_{ij} = \frac{1}{2}\left(\frac{\partial u_i}{\partial x_j} + \frac{\partial u_j}{\partial x_i}\right) \tag{2.4}$$

• Energy

$$\frac{\partial(\rho E)}{\partial t}+\frac{\partial(\rho u_i E)}{\partial x_j}=-\frac{\partial(p u_i)}{\partial x_i}+\frac{\partial}{\partial x_j}\left(\tau_{ij}u_i-q_i\right) \tag{2.5}$$

where E is the total energy of the fluid and is given by

$$E=\rho\left(e+\frac{1}{2}u_i u_i\right). \tag{2.6}$$

The heat flux vector, q_i is given by Fourier's Law and is given by,

$$q_i=-k_T\frac{\partial T}{\partial x_i}. \tag{2.7}$$

where k_T is the heat transfer coefficient.

The equations of state for a perfect gas is given by

$$P=\rho RT. \tag{2.8}$$

where R is the specific gas constant.

This set of equations provides a complete description of the three-dimensional newtonian fluid flows considered in this dissertation.

2.3 Turbulence Modeling

2.3.1 Reynolds Averaging Approach

Reynolds averaging is used to simplify Navier-Stokes equations by decomposing the instantaneous flow into a mean flow and turbulent fluctuations, which is known as the Reynolds decomposition, as follows

$$u_i=U_i+u_i'. \tag{2.9}$$

where U_i is the mean flow velocity and u_i' is the fluctuating velocity due to turbulence.

By substituting into Navier-Stokes equations then taking the average, the Navier-Stokes equations for incompressible flow reduce to

$$\rho\frac{\partial\overline{U_i}}{dt}+\rho\frac{\partial\overline{U_iU_j}}{\partial x_j}=-\frac{\partial\bar{P}}{\partial x_i}+\frac{\partial}{\partial x_j}\left(\bar{\tau}_{ij}+\tau_{ij}^{R}\right)+\rho f_i. \tag{2.10}$$

Boussinesq's approximation assumes that the anisotropic Reynolds stresses, (a_{ij} = $\overline{u_i'u_j'}$-2/3 $k\delta_{ij}$) are proportional to the mean strain rate and can be expressed as,

$$a_{ij}=-2\mu_T\bar{S}_{ij}. \tag{2.11}$$

This introduces a viscosity parameter, known as the turbulent eddy viscosity, μ_T. As the Reynolds stresses also include an isotropic part, Boussinesq's eddy viscosity approximation becomes,

$$\tau_{ij}^{R}=-\rho\overline{u_i'u_i'}=2\mu_T\bar{S}_{ij}-\frac{2}{3}\rho k\delta_{ij} \tag{2.12}$$

where k is the specific turbulent kinetic energy of the turbulent fluctuations, given by:

$$k=\frac{u_i'u_i'}{2}. \tag{2.13}$$

There are two assumptions being made in Boussinesq's approximation: 1) The anisotropic Reynolds stresses can be defined at each point in space and time by the mean velocity gradients and 2) The turbulent eddy viscosity is a scalar property of the flow, meaning that the relationship between the anisotropy and the velocity gradient is linear. For a more detailed explanation refer to [65, 50].

2.4 Application of Turbulence Models to Delta Wing Vortical Flows

The velocity gradients of the flow are the components of a second-order tensor and can be resolved into isotropic, symmetric-deviatoric and anti-symmetric parts [65]. The decomposition is shown in Equation 2.14 where the strain rate tensor, S_{ij}, is the symmetric-deviatoric part, and the rotation tensor, Ω_{ij}, is the anti-symmetric-deviatoric part,

$$\frac{\partial u_i}{\partial x_j} = \frac{1}{3}\frac{\partial u_k}{\partial x_k}\delta_{ij} + S_{ij} + \Omega_{ij} . \tag{2.14}$$

The strain-rate tensor was defined in Eq. 2.4 and the rotation tensor is given by,

$$\Omega_{ij} = \frac{1}{2}\left(\frac{\partial u_i}{\partial x_j} - \frac{\partial u_j}{\partial x_i}\right). \tag{2.15}$$

The rotation tensor is related to the vorticity of the flow,

$$\omega_i = -\varepsilon_{ijk}\Omega_{jk} \tag{2.16}$$

where ε_{ijk} is the alternating symbol.

The product of the velocity gradient and the Reynolds stress tensor is the production of turbulent kinetic energy,

$$P_k = \tau_{ij}^R \frac{\partial \overline{U_i}}{\partial x_j}. . \tag{2.17}$$

Four Turbulence models will be presented in the following sections.

2.4.1 Wilcox $k-\omega$ Model

Wilcox [50 and 51] proposed the $k-\omega$ two equation turbulence model which is based on Boussinesq's approximation. Two flow parameters are utilized to calculate the eddy viscosity, k, specific turbulent kinetic energy and, ω, the specific dissipation rate per unit turbulent kinetic energy. The kinematic eddy viscosity for this model is given by

$$\mu_T = \rho\frac{k}{\omega}. \tag{2.18}$$

Two transport equations are added to the Navier-Stokes equations in the solution of the flow. The transport equation for the turbulent kinetic energy is given as

$$\underbrace{\rho\frac{\partial k}{\partial t} + \rho\frac{\partial kU_j}{\partial x_j}}_{Convection} = \underbrace{\frac{\partial}{\partial x_j}\left[\left(\mu + \sigma^*\mu_t\right)\frac{\partial k}{\partial x_j}\right]}_{Diffusion} + \underbrace{P_k}_{\text{Production}} - \underbrace{\beta^*\rho k\omega}_{Dissipation} \tag{2.19}$$

Eq. 2.19 includes convection, diffusion, production and destruction terms as indicated, so it is similar in form to the momentum equations given in Equation 2.2. The transport equation for the dissipation, ω, takes a similar form and is given in Ref [50]. To understand how this model applies to delta wing vortical flows, it is necessary to consider the production terms. The production of the turbulent kinetic energy was defined in Eq. 2.17 and the corresponding term for the dissipation rate is given as

$$P_\omega = \alpha \frac{\omega}{k} P_k. \tag{2.20}$$

As mentioned, this model uses Boussinesq's approximation to calculate the Reynolds stresses and, therefore, the production term is expanded to become

$$P_k = 2\mu_T \bar{S}_{ij} \bar{S}_{ij}. \tag{2.21}$$

Based on Eq. 2.20 and 2.21, the production of k and ω within this model are only dependent on the mean strain-rate of the flow. No rotation rate was taken into account. This simplification of the model results in a large over-production of turbulence within the vortex core. This over-production of turbulence causes the model to predict exaggerated levels of vorticity diffusion. This results in the prediction of a weak vortex.

2.4.2 Non-Linear Eddy Viscosity Model (NLEVM)

To model the Reynolds stresses, the non-linear eddy viscosity model (NLEVM) is introduced. The NLEVM is based on the Wilcox $k-\omega$ model and uses the formulation of an explicit algebraic Reynolds stress model proposed by Wallin, Johansson [48], and Hellsten [49].

An extra term is introduced to the calculation of the anisotropic Reynolds stresses as defined by Boussinesq's approximation,

$$a_{ij} = -2\mu_T \bar{S}_{ij} + a_{ij}^{(ex)}. \tag{2.22}$$

The extra term $a_{ij}^{(ex)}$ creates a non-linear relationship for the Reynolds stresses due to its dependence on both the mean strain rate and rotational tensors. The equation for the Reynolds stresses then will be

$$\overline{u_i' u_j'} = k\left(\frac{2}{3}\delta_{ij} - 2\mu_T \bar{S}_{ij} + a_{ij}^{(ex)}\right). \quad (2.23)$$

In this model, the mean strain rate and rotation tensors are normalized by the turbulent time scale, τ , i.e. $S = \tau \bar{S}_{ij}$ and $\Omega = \tau \bar{\Omega}_{ij}$, where

$$\tau = \max\left\{\frac{1}{\beta^* \omega}, C_\tau \sqrt{\frac{\mu}{\beta^* k \omega}}\right\}. \quad (2.24)$$

The extra anisotropy term is a reduction of the general form of a_{ij} used in explicit Reynolds stress models, and contains ten tensorally independent terms. The reduced form, with tensor subscripts omitted, is

$$a^{(ex)} = \beta_3\left(\Omega^2 - \frac{1}{3} II_\Omega \, I\right) + \beta_6\left(S\Omega^2 + \Omega^2 S - II_\Omega S - \frac{2}{3} IV \, I\right) + \beta_9(\Omega S \Omega^2 - \Omega^2 S \Omega) \quad (2.25)$$

where I is the identity matrix. II_Ω and IV are two of the independent invariants of S and Ω .The model constants are detailed in Ref [49].

In addition to introducing this new anisotropic term, the calculation of the turbulent eddy viscosity is also modified from the $k - \omega$ model and takes the following form,

$$\mu_T = C_\mu^{eff} \rho k \tau \quad (2.26)$$

where

$$C_\mu^{eff} = -\frac{1}{2}(\beta_1 + II_\Omega \beta_6). \quad (2.27)$$

From this definition of the turbulent eddy viscosity it is clear that the behavior of the rotation tensor is also taken into account.

To consider the behavior of this model in the prediction of vortical flows, the production of turbulence should again be considered. This also now has an additional term and takes the following form,

$$P_k = \left(2\mu_T \bar{S}_{ij} - a_{ij}^{(ex)}\right)\bar{S}_{ij}. \tag{2.28}$$

From this relationship, the extra term clearly acts to reduce the turbulent production from the original model. The value of the extra anisotropy will increase and, therefore, reduce the turbulence within the vortex core. The levels of turbulent eddy viscosity also decreases in this region, further reducing the levels of turbulence in the flow.

2.4.3 Spalart-Allmaras Model

A single equation for a working variable $\tilde{\nu}$ in the one-equation Spalart-Allmaras model [58] is based on Boussinesq's approximation. The $\tilde{\nu}$ term is related to the turbulent eddy viscosity of the flow by the following relationship

$$\mu_T = \rho\tilde{\nu} f_{v1}. \tag{2.29}$$

The single differential equation which defines this model was derived empirically using arguments based on dimensional analysis, invariance, and molecular viscosity. The origin of each term is described in detail in Ref. [58]. The transport equation for the undamped eddy viscosity, $\tilde{\nu}$, is given as

$$\underbrace{\frac{\partial \tilde{\nu}}{\partial t} + \frac{\partial\left(\tilde{\nu} u_j\right)}{\partial x_j}}_{Convection} = \underbrace{c_{b1}\tilde{\nu}\tilde{S}}_{\text{Production}} - \underbrace{c_{w1} f_w \left(\frac{\tilde{\nu}}{d}\right)^2}_{Dissipation} + \underbrace{\frac{1}{\sigma}\frac{\partial}{\partial x_k}\left[\left(\nu + \tilde{\nu}\right)\frac{\partial \tilde{\nu}}{\partial x_k}\right] + \frac{c_{b2}}{\sigma}\frac{\partial \tilde{\nu}}{\partial x_k}\frac{\partial \tilde{\nu}}{\partial x_k}}_{Diffusion} \tag{2.30}$$

where

$$f_{v1} = \frac{\chi^3}{\chi^3 + c_{v1}} \tag{2.31}$$

$$\chi = \frac{\tilde{\nu}}{\nu} \tag{2.32}$$

$$\tilde{S} = S + \frac{\tilde{\nu}}{k^2 d^2} f_{v2} \tag{2.33}$$

$$f_{v2} = 1 - \frac{\chi}{1+\chi f_{v1}} \tag{2.34}$$

$$S = \sqrt{2\Omega_{ij}\Omega_{ij}} \tag{2.35}$$

where C_{v1}, and k are constants, d is the distance from wall, v is the molecular viscosity and S is a scalar measure of the deformation tensor and is based on the magnitude of the vorticity. All model coefficients and definitions are detailed in Ref [58]. Ω_{ij} is given by Equation 2.15.

As previously indicated, the general form of the equation is similar to the momentum equations given by Equation 2.2 and includes convection, diffusion, production, and destruction terms. The wall destruction term is derived to reduce the turbulent viscosity in the laminar sublayer.

After calculating the turbulent eddy viscosity using the transport equation, Boussinesq's approximation is used to determine the Reynolds stresses and close the Navier-Stokes equations. As a Boussinesq's approximation based model, the Spalart-Allmaras model suffers from the same problems as the standard Wilcox k–ω model discussed previously. Due to the use of the strain-rate tensor in the calculation of the Reynolds stresses, the model may predict unrealistic contributions of the Reynolds stresses in regions of high rotational flow such as the vortex core.

2.4.4 Spalart-Allmaras Model with Rotation and Rotation/Curvature Corrections (SARRC)

Corrections proposed to enable the SA turbulence model to predict the vortical flow behavior were the rotation and rotation/strain. Both of these corrections will be used in

this dissertation.

2.4.4.1 Spalart-Allmaras Model with Rotation Correction (SAR)

Mariani *et al.* [59 and 60] proposed a correction for the SA model to reduce the turbulent eddy viscosity in high rotational flows such as a vortical flow. The reduction in the eddy viscosity production was done by reducing the production of eddy viscosity where the measure of vorticity was greater than the strain rate. In this modification, Equation 2.35 is replaced by

$$S = |\Omega_{ij}| + C_{prod} \min(0, |S_{ij}| - |\Omega_{ij}|) \tag{2.36}$$

where

$$C_{prod} = 2.0, |\Omega_{ij}| = \sqrt{2\Omega_{ij}\Omega_{ij}}, |S_{ij}| = \sqrt{2S_{ij}S_{ij}} \tag{2.37}$$

and S_{ij} is given by Equation 2.4.

To select this correction in the fluid solver used herein, ANSYS Fluent, the Strain/Vorticity production option was chosen under the Spalart-Allmaras production in the Spalart-Allmaras turbulence model dialogue box [66].

2.4.4.2 Spalart-Allmaras Model with Rotation/Curvature Correction (SARC)

A modification of the production term $C_{b1}\tilde{\nu}\tilde{S}$ for the SA model were proposed by Spalart and Shur [61] and Shur *et al.* [62] to account for the rotation and curvature by reducing the turbulent eddy viscosity in regions with high vorticity. The modification includes multiplying the production term $C_{b1}\tilde{\nu}\tilde{S}$ of the SA model by the rotation function, f_{r1},

$$f_{r1} = (1 + c_{r1})\frac{2r^*}{1+r^*}(1 - c_{r3}\tan^{-1}(c_{r2}\tilde{r})) - c_{r1} \tag{2.38}$$

where

$$r^* = \frac{S}{\Omega} = \frac{\sqrt{2S_{ij}S_{ij}}}{\sqrt{2\Omega_{ij}\Omega_{ij}}} = \sqrt{\frac{S_{ij}S_{ij}}{\Omega_{ij}\Omega_{ij}}} \tag{2.39}$$

$$\tilde{r} = \frac{2\Omega_{ik}S_{jk}}{\tilde{D}}\left[\frac{DS_{ij}}{Dt} + \left(\varepsilon_{imn}S_{jn} + \varepsilon_{jmn}S_{in}\right)\Omega_m^{Rot}\right] \tag{2.40}$$

$$\tilde{D} = D^4 = \left[\left(S_{ij}S_{ij} - \Omega_{ij}\Omega_{ij}\right)\right]^2 \tag{2.41}$$

S_{ij} is given by Equation 2.4, and Ω_{ij} in Equation 2.15 is modified as follows,

$$\Omega_{ij} = \frac{1}{2}\left(\frac{\partial u_i}{\partial x_j} - \frac{\partial u_j}{\partial x_i}\right) + 2\varepsilon_{mji}\Omega_m^{Rot} \tag{2.42}$$

DS_{ij}/Dt are the components of the Lagrangian derivative of the strain rate tensor and all the derivatives should be defined with respect to the reference frame Ω^{Rot}. The reference frame Ω^{Rot} should be used only if the reference frame itself is rotating. To select this correction in the fluid solver used herein, ANSYS Fluent, the curvature correction under option was chosen in the Spalart-Allmaras turbulence model dialogue box [66].

2.5 Computational Formulation

2.5.1 Fluid Solver

The commercial ANSYS Fluent software (version 14.0) [67] is used in the simulations conducted in this dissertation. The Finite Volume approach is used to discretize the computational field with a structured grid with a collocated cell centered variable arrangement. Second order discretization of the momentum equations is employed. The diffusive terms are discretized using a second-order central-difference scheme. For the convective term a second-order finite-difference scheme is implemented. The pressure-velocity coupling algorithm has been utilized for the pressure-velocity coupling [68], with an implicit, second order scheme [69 and 70].

Two turbulence models are used in this dissertation. The two turbulence models are the modified Spalart-Allmaras model (SARRC) with a rotation/curvature based production and curvature treatment, and the Non-linear Eddy Viscosity Model (NLEVM)

turbulence model. Both SARRC and NLEVM turbulence models are in ANSYS software. The SARRC turbulence model can be selected in ANSYS Fluent by choosing the SA turbulence model with strain/vorticity based production and curvature correction option as shown in Table 2.1. The NLEVM turbulence model can be selected in ANSYS Fluent by choosing $k-\omega$ model with WJ-BSL-EARSM option as shown in Table 2.2. For more information about the coding and using SARRC and NLEVM turbulence model options, refer to ANSYS Fluent Theory Guide [66].

Table 2.1. SARRC Turbulence model Dialogue Box selections in the fluid solver.

	Selection
Turbulence Model	Spalart-Allmaras (1 eqn)
Spalart-Allmaras Production	Strain/Vorticity Based
Options	Curvature correction is checked

Table 2.2. NLEVM dialogue box in the fluid solver.

	Selection
Turbulence Model	k-omega (2 eqn)
k-omega model	WJ-BSL-EARSM

2.5.2 Structural Solver

Finite element analysis is used in this dissertation to model the two tails. The aeroelastic equations of motion of the vertical tails are given by

$$[M]\{\ddot{U}\} + [C]\{\dot{U}\} + [K]\{U\} = [F] \tag{2.43}$$

where:

[M] = structural mass matrix

[C] = structural damping matrix

[K] = structural stiffness matrix

$\{\ddot{U}\}$ = nodal acceleration vector

$\{\dot{U}\}$ = nodal velocity vector

{U} = nodal displacement vector

[F] = applied load vector due to Aerodynamic Loads

"ANSYS Mechanical" software was used in this simulation. The tail movement involves coupled bending and torsional oscillations. Therefore, shell elements were used in the structural simulations for the vertical tail of the F/A-18 aircraft. The shell element type used in this dissertation is SOLID186 elements. The SOLID186 element is a higher order, three-dimensional 20-node solid element; more details can be found in Ref. [71]. Also, in the present simulations, no structural damping was used and the consistent mass matrix was used. Consistent mass matrix leads to more accurate solutions, because it is constructed using the interpolation function used to describe the displacement field and thus is consistent with that of the stiffness matrix.

In the present simulations, linear solver is considered adequate. There are two types of non-linear structural dynamics that might have been applied for the present problem (there is no contact non-linearity in this simulation): material non-linearity and geometry (large displacement) non-linearity. The material used in the structural analysis for the tails are wood and aluminum. Both wood and aluminum have constant moduli of elasticity. Therefore, there is no need to use non-linear solver for theses linear materials. For the displacement simulation results, the displacement is far too small. The largest displacement ratio (max displacement/ max dimension of the tail) obtained during simulations is 2%, which is less than 5% (the threshold to use non-linear structural solver). Therefore, the stiffness matrix will be constant and it will not be a function of the

displacement.

The structural solver supports two time integration algorithms, implicit and explicit. The implicit time integration methods in ANSYS are Newmark and Generalized-α. Implicit method is unconditionally stable. There are no restrictions on the time step. The time step size can vary to satisfy the time-accuracy requirement. Implicit methods require the inversion of the *stiffness* matrix. The Generalized-α method covers WBZ- α, HHT- α methods. The generalized-α method is useful in non-linear structural dynamics simulations and high frequency simulation problems incorporating many degrees of freedom, and in which it is desirable to numerically attenuate (or dampen-out) the response at high frequencies. The generalized-α method has a numerical dissipation controlled by two parameters which should affect higher modes; lower modes should not be affected. The Newmark method controls the numerical dissipation with one parameter only. By selecting δ=0.5, α =0.25; the Newmark method is called the constant average method and it does not induce any numerical dissipation in the solution. Explicit time integration method in ANSYS is the central difference time integration. Explicit methods are usually used for short-time, large, quasi-static problems with large deformations and multiple nonlinearities, and complex contact/impact problems, such as drop tests. Explicit methods are only conditionally stable; they require very small time step to maintain the stability limit. Explicit methods require the inversion of the mass matrix.

In the present simulations, the Newmark time integration implicit method is used, because the structural simulations in this dissertation are linear. Moreover, the main natural frequency, affecting the structure, is the first bending natural frequency, so there

is no need to need to attenuate the higher frequencies. The Newmark implicit method does not have a numerical stability limitation on the time step.

2.5.3 Fluid-Structure Interaction

The normal and tangential force was transmitted by the conservative and consistent fluid-structure interface algorithm to the tails and the deflections of the tail was transmitted back to the fluid. The interfaces transmit the normal and tangential forces from the fluid grid to the structure grid in a conservative manner. Therefore, the sum of all forces on the structure grid interface is equivalent to the sum of all forces on the fluid grid interface. Each data transfer incorporates two algorithmic components: Mapping and Interpolation.

• Mapping involves the matching and pairing of a source and a target location to generate weights. Every fluid node must be mapped to a solid element to receive displacements. Similarly, each structural mesh node in a solid element must be mapped to a fluid element to receive the force value.

• Interpolation involves the use of the generated weights to project source data onto target locations. More details can be found in Ref. [72].

2.5.4 Grid Motion Module

The fluid grid deforms at each time step to accommodate the deformed tails. The six outer boundary surfaces of the computational domain are kept fixed. The grid is deformed using the dynamic mesh option in the fluid solver. More information can be reviewed in Ref. [72].

The experimental data used in this dissertation will be presented in the next section.

2.6 Experimental Data

The experimental data used in this dissertation for comparison is by Washburn [26]. Washburn utilized a simplified geometry of subsonic flow at a Mach number 0.3 over a 76-deg delta wing at 30-deg angle of attack. Two vertical tails were placed downstream of the delta wing. Each tail is modeled as a single aluminum spar covered with balsa wood covering, as shown in Figure 2.1. The aluminum spar is constructed from a 6061-T6 alloy. The tail construction can be reviewed in Ref [40 and 26]. The pressure transducer locations on the right tail in the fluid solver are shown in Figure 2.2. A schematic of the two vertical tails is shown in Figure 2.3.

The element selection and grid details, for structural and fluid domains, used in this dissertation will be presented in the next section.

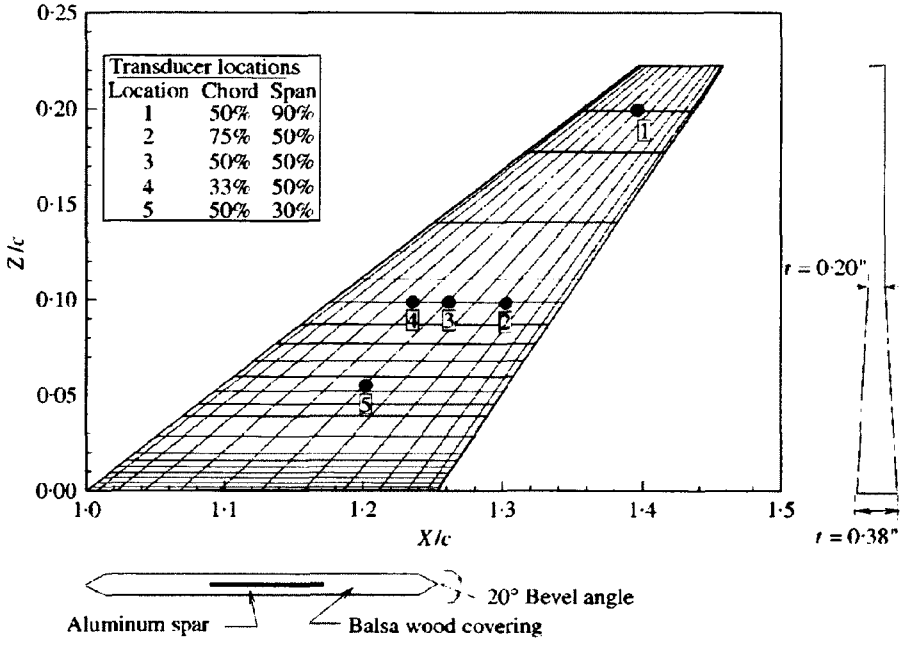

Figure 2.1. Schematic view of the vertical tail construction and dimensions [37].

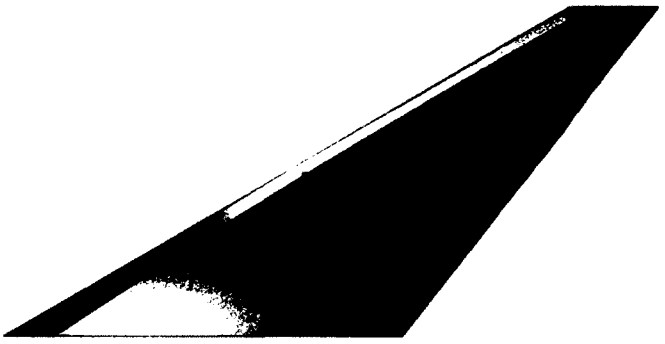

Figure 2.2. The pressure transducer locations on the tail in the fluid solver.

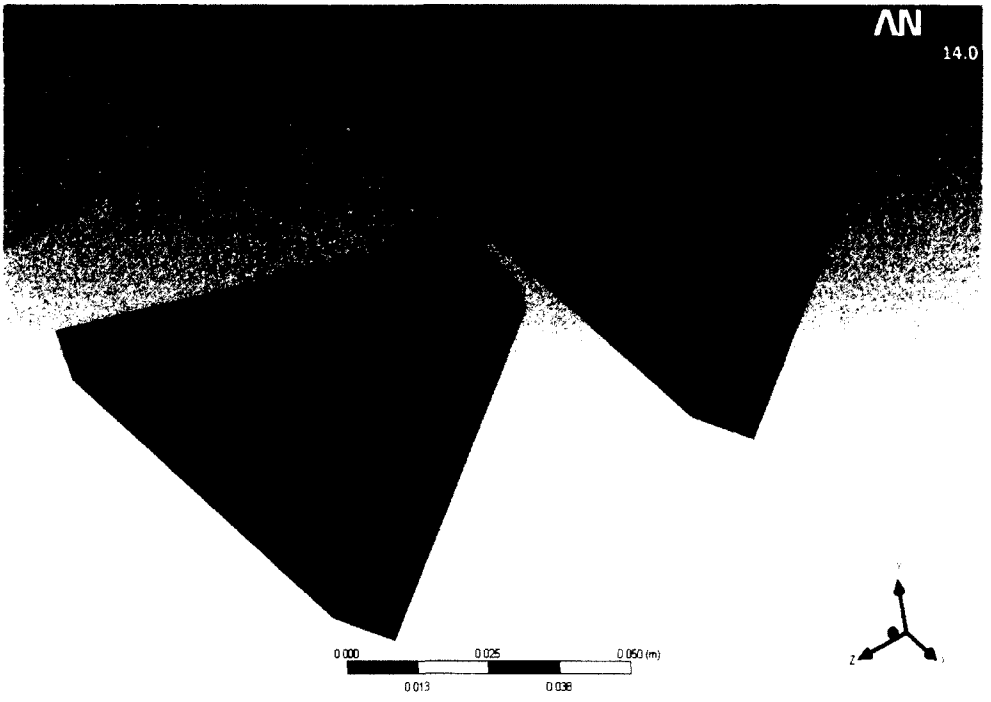

Figure 2.3. The two vertical tail schematic used in the structural solver.

2.7 Mesh Details

2.7.1 Structural Dynamics Mesh

A mesh dependency study was performed using 3 different meshes. Table 2.3 shows the maximum deflection and Von-Mises stress for 3 different grids. The second mesh was selected for the present simulations due to its convergence with the third mesh. The

unstructured mesh consists of 200,411 elements. The structural mesh of the tail and the CFD cell projection on the tail is shown in Figure 2.4 and 2.5, respectively.

Table 2.3. Structural mesh dependency study results.

	Grid 1	Grid 2	Grid 3
Number of elements	8233	200411	537339
Number of Nodes	15785	341394	834694
Max total deformation (mm)	1.643	1.658	1.66
Max Von-Mises stress (Mpa)	6.3836	6.3053	6.3234

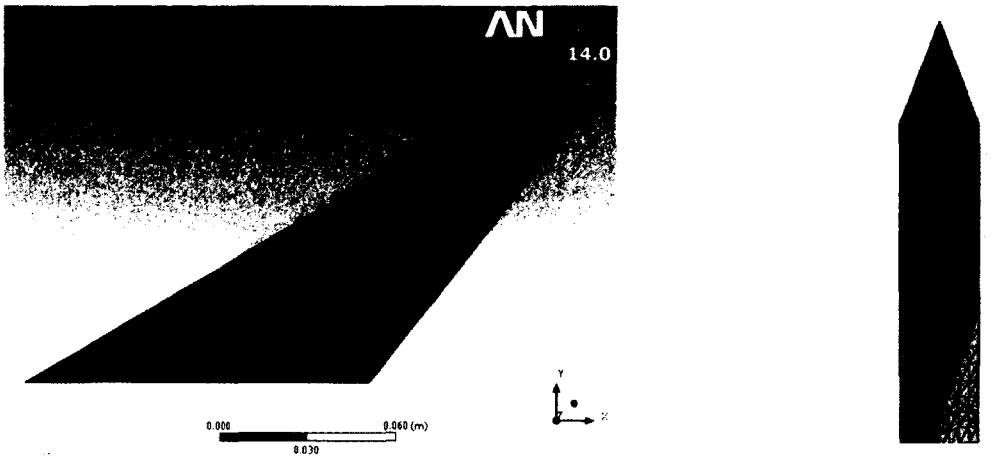

Figure 2.4. Structural mesh of the tail in the structural solver.

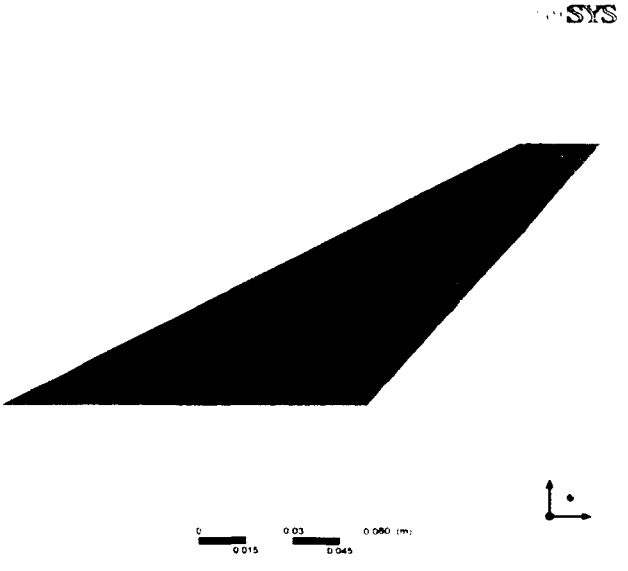

Figure 2.5. Fluid mesh projection on the tail in the solver.

2.7.2 Fluid Dynamics Mesh

A mesh dependency study was conducted using two meshes of varying cell number. Each mesh was processed using the NLEVM turbulence model and steady-state case for 300 iterations. The first mesh consists of 3,807,924 elements. The refined mesh consists of 4,297,360 elements. A comparison of the pressure on the wing upper surface at a distance of 0.13 m from the tip for both meshes is shown in Figure 2.6. From Figure 2.6, no further refinement was required. The mesh of 3,807,924 elements will be used in the present simulation.

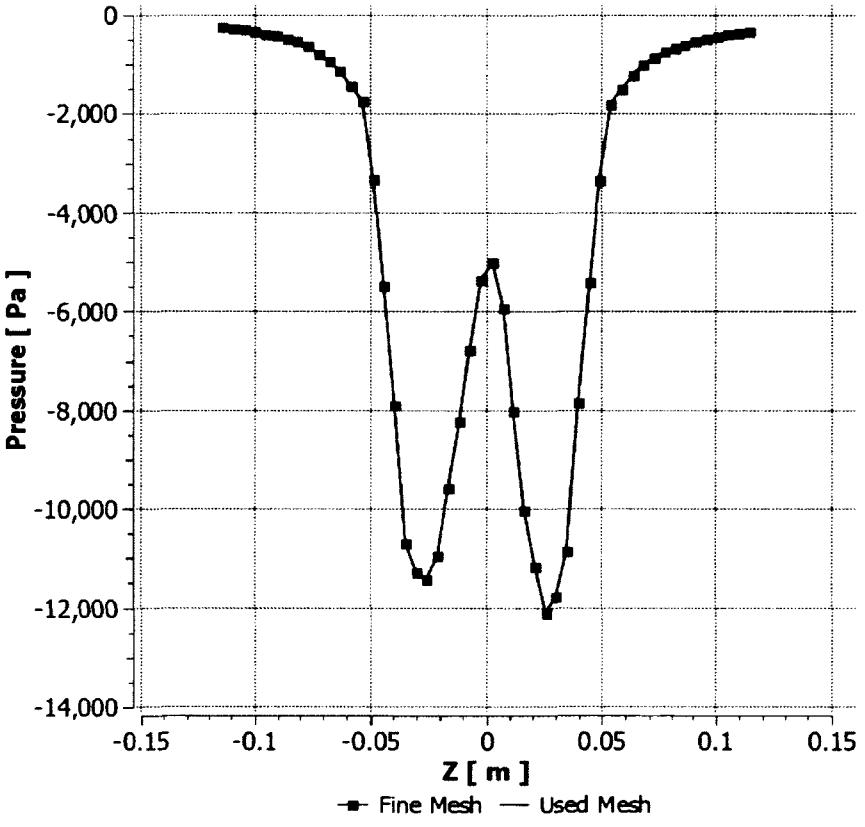

Figure 2.6. Fluid mesh comparison of the pressure distribution on the upper surface of the wing at a distance of 0.13716 m from the wing tip. One-way fluid-structure interaction case.

A time step study was conducted. Two time steps were used. Figure 2.7 shows the amplitude difference between the two time steps: 10^{-3} and 5×10^{-4} sec. Figure 2.7 shows a similarity in the frequency of the cycles and different amplitudes with a max deviation of 20%. Other researchers [40 and 41] recommend a time step of 10^{-5} sec. A time step of 10^{-3} sec was utilized in this dissertation for a total time of 0.1 sec. This time step was chosen to demonstrate the amount of fidelity that can be achieved by the investigator by optimizing the available computational power.

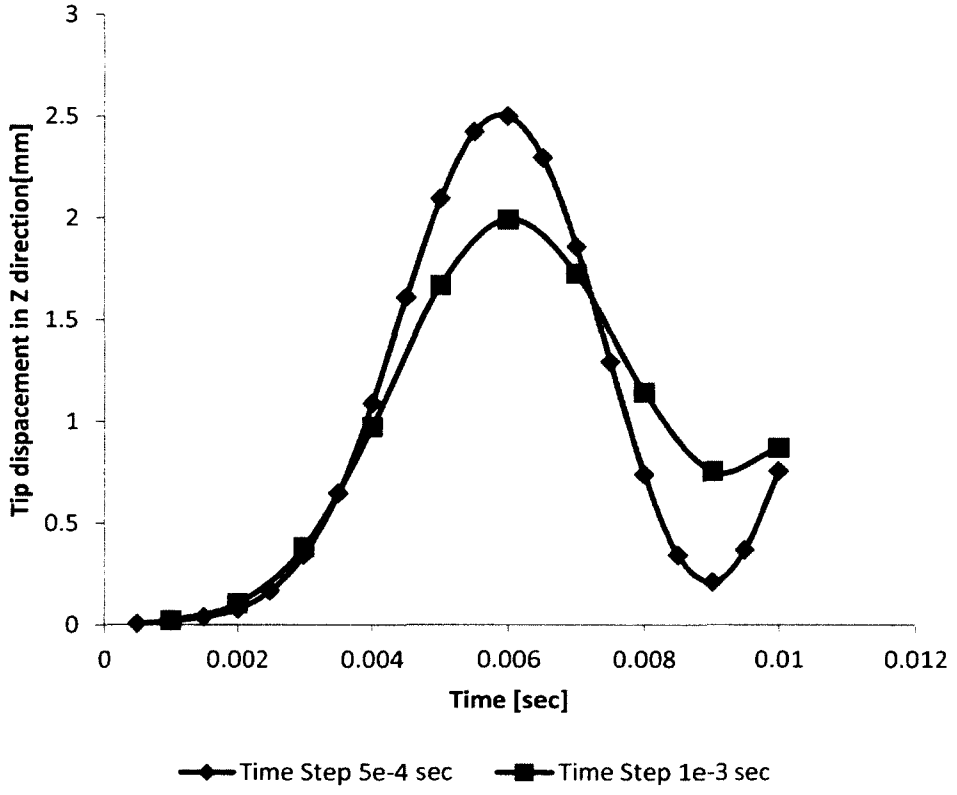

Figure 2.7. Time step check study. Two-way fluid-structure interaction case.

The used CFD mesh is a multi-block of unstructured grids consisting of 3 blocks. Finer meshes were used in the tail and wing area because this is the area where the vortices above the wing formed and hit the two vertical tails. The computational grid,

generated by ANSYS ICEM CFD mesh generation software for the fluid solver is shown in Figures 2.8, 2.9, 2.10 and 2.11.

The 76-deg delta-wing/twin-tail configuration used in the fluid solver is at an angle of attack of 30-deg, a subsonic flow of a Mach number 0.3 and a Reynolds number of 3.7×10^{6}.

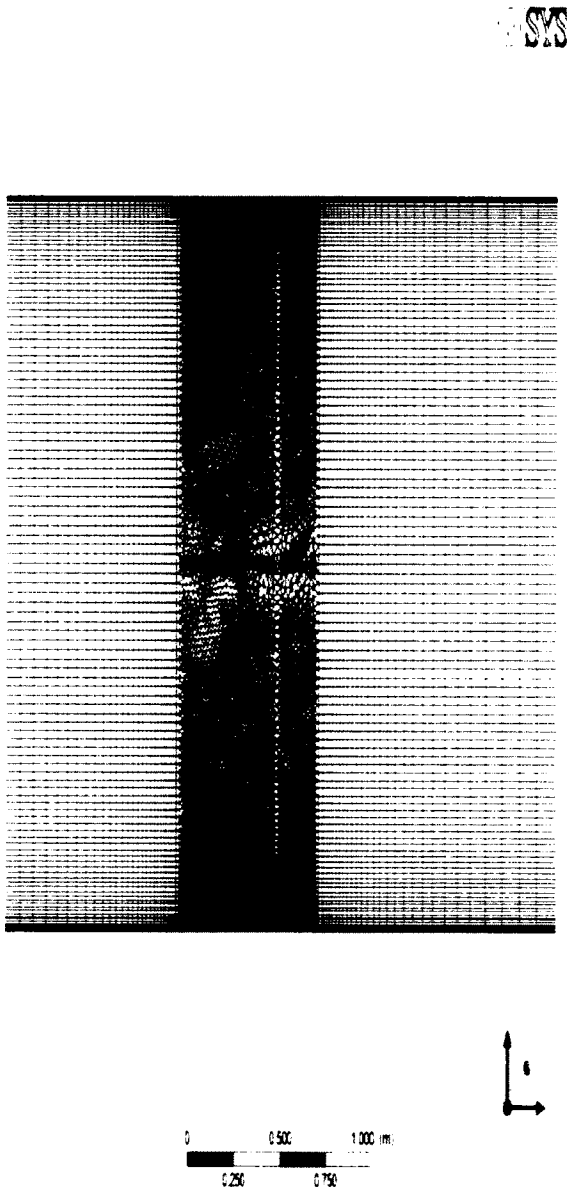

Figure 2.8. Fluid mesh. Full symmetry z-plane view of the delta wing/twin-tail configuration.

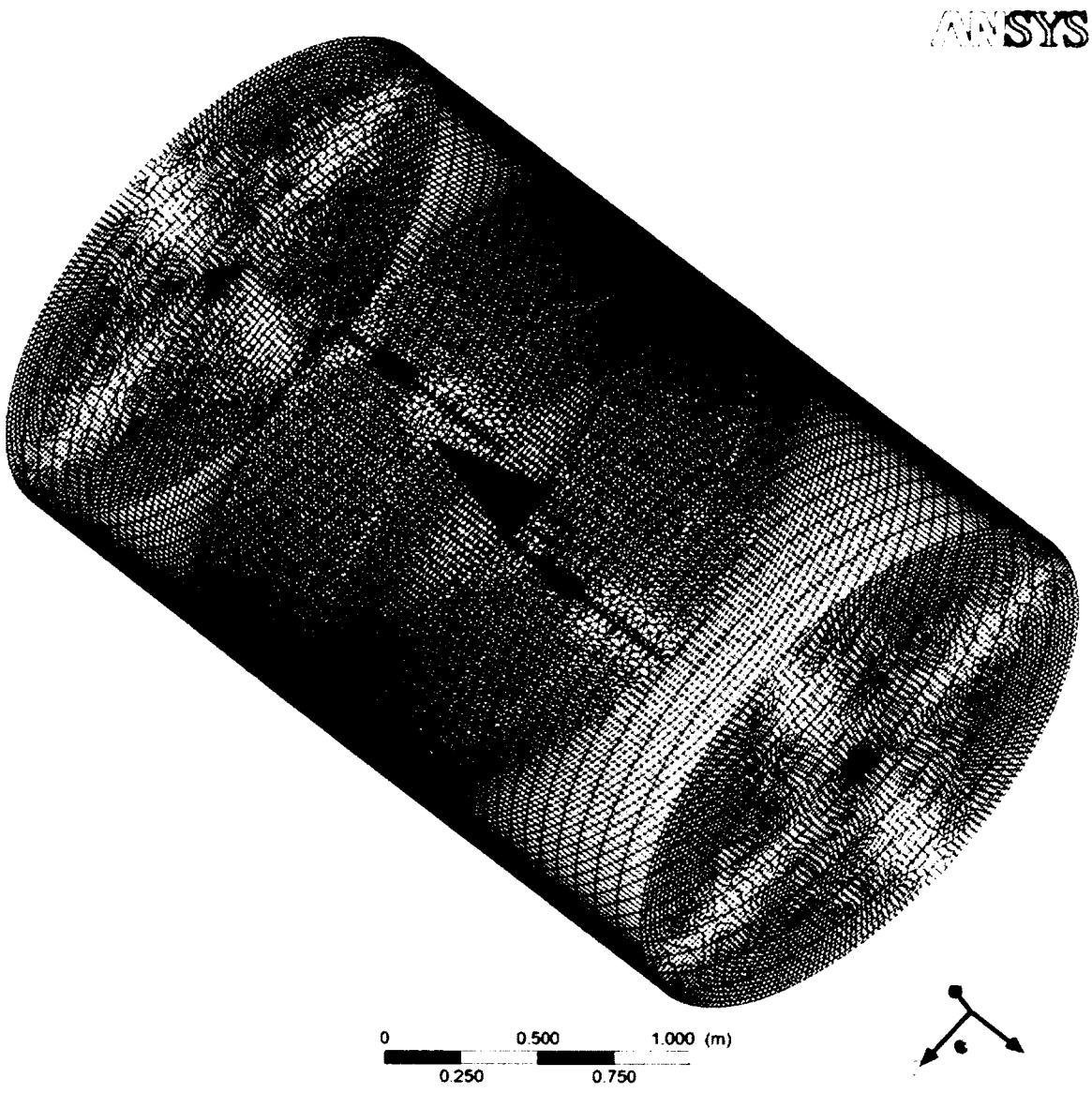

Figure 2.9. Fluid mesh. Three-dimensional view of the delta wing/twin-tail configuration.

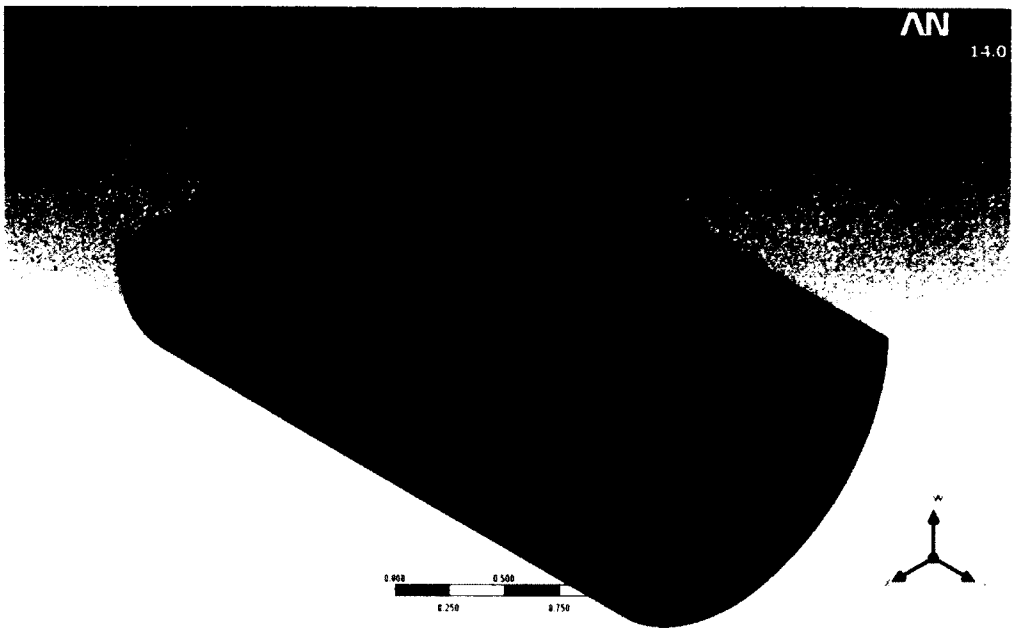

Figure 2.10. Fluid mesh. Full symmetry y-plane view of the delta wing/twin-tail configuration.

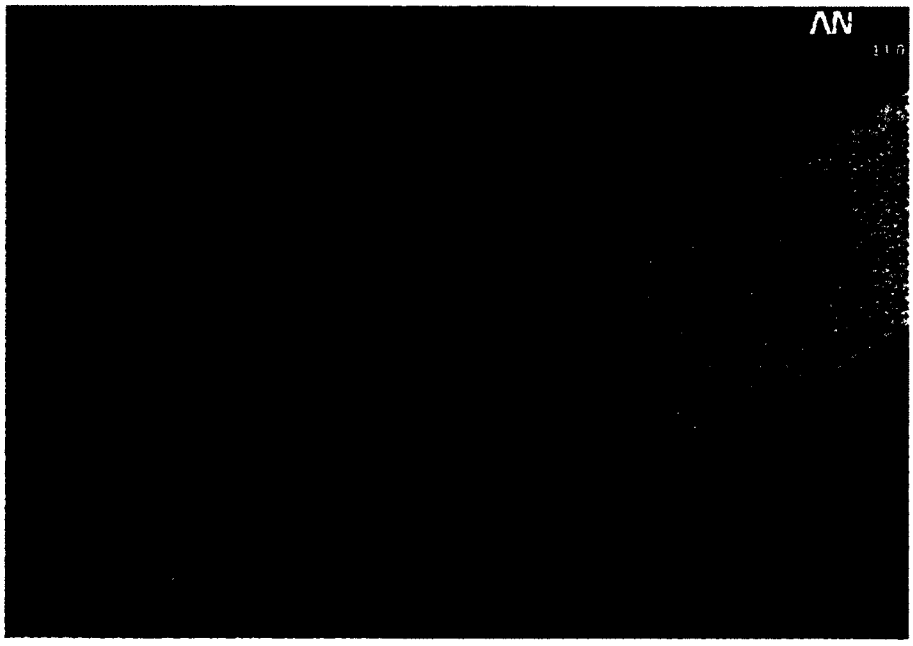

Figure 2.11. Fluid mesh. Three-dimensional close-up view of the delta wing/twin-tail configuration.

2.8 Summary

The advantages of the two non-linear NLEVM and SARRC turbulence models were demonstrated and compared to the standard Wilcox $k-\omega$ and Spalart-Allmaras turbulence models; respectively. Both SARRC and NLEVM turbulence models depend more on rotation and strain-rate which lead to improved pressure values at the vortex core. The two non-linear NLEVM and SARRC turbulence models depend more on both rotation and strain-rate. Therefore, NLEVM and SARRC turbulence model were utilized in the simulations conducted in this dissertation to simulate the vortical flow above a delta wing and the associated tail buffet.

The following chapter shows the simulation results conducted by using ANSYS. The simulation was conducted by using a steady-state a one-way fluid-structure interaction and an unsteady two-way fluid-structure interaction for the tail buffet of simplified geometry of a F/A-18 fighter.

CHAPTER 3

RESULTS AND DISCUSSION OF RESULTS

In this chapter, the simulation results for the vortical flow over a delta wing are presented. Computed pressure values on the tail surface were compared with the experimental data conducted by Washburn [26]. The simulations were conducted by using a simplified geometry of Washburn [26]. Two vertical tails were placed downstream of the delta wing. The simulations were conducted for the following flow conditions: subsonic flow at a Mach number 0.3 and a Reynolds number of 3.7×10^6 over a 76-deg, sharp-edged, delta wing at 30-deg angle of attack. The simulations were conducted on an Intel Core 2 Duo 2.66 GHz processor and 16GB RAM computer.

3.1 Results for Steady RANS, One-Way Fluid-Structure Interaction Case

In one-way fluid structure interaction simulation, the fluid domain solver ANSYS Fluent ran first until a converged solution is obtained. The fluid domain converged solution was used as an external force to the structural domain solver ANSYS Mechanical. Then, the structural domain solver ANSYS Mechanical runs until a converged solution was obtained. No marching in physical time was conducted in the steady one-way fluid structure interaction simulations.

The steady one-way fluid structure interaction simulations were conducted to confirm that the simulation code was able to predict the main flow features. Due to the unsteady nature of the physical flow and the movements of the tails effect on the flow, which were not considered in these steady RANS, one-way fluid-structure interaction computations, large errors in pressure value prediction near the vortex cores were expected.

Four cross planes used to plot the total pressure contours are shown in Figure 3.1.

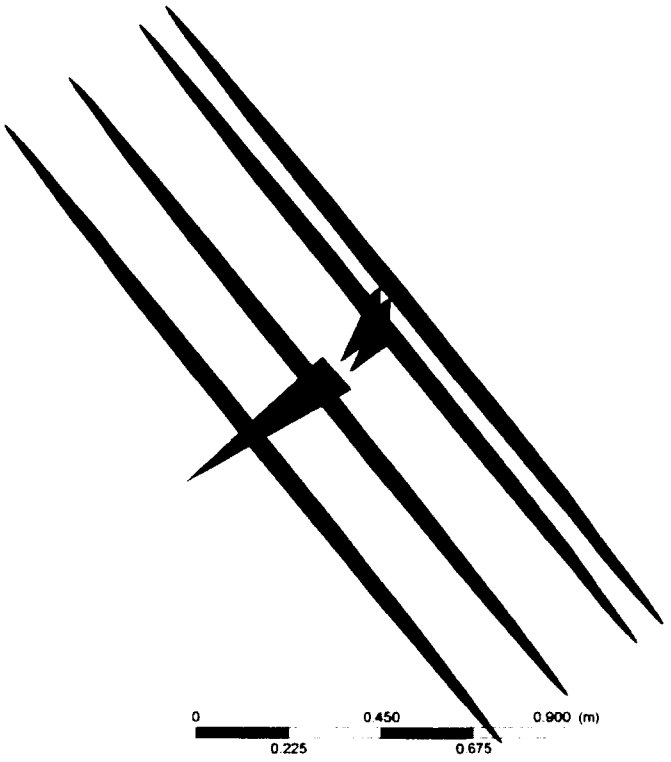

Figure 3.1. Cross planes location used to plot total pressure contours.

Presented in Figure 3.2 are comparisons of the SARRC- and NLEVM–computed vortex core trajectories with experimental data. There is a good agreement with a maximum difference of 14% between the experimental and numerical data for the trajectories of the vortex core. No previous comparisons were conducted for the vortex core trajectories with experimental data by other researchers listed in the literature review chapter.

Figures 3.3 and 3.4 show the total pressure contours for the upper surface of the wing using SARRC and NLEVM turbulence models. Figures 3.3 and 3.4 show the extent of the vortex and that the agreement between SARRC and NLEVM is fairly good. The increase of the total pressure indicates the vortex breakdown. The breakdown of the two

vortices is symmetric. The vortex breakdown locations are almost the same for both turbulence models.

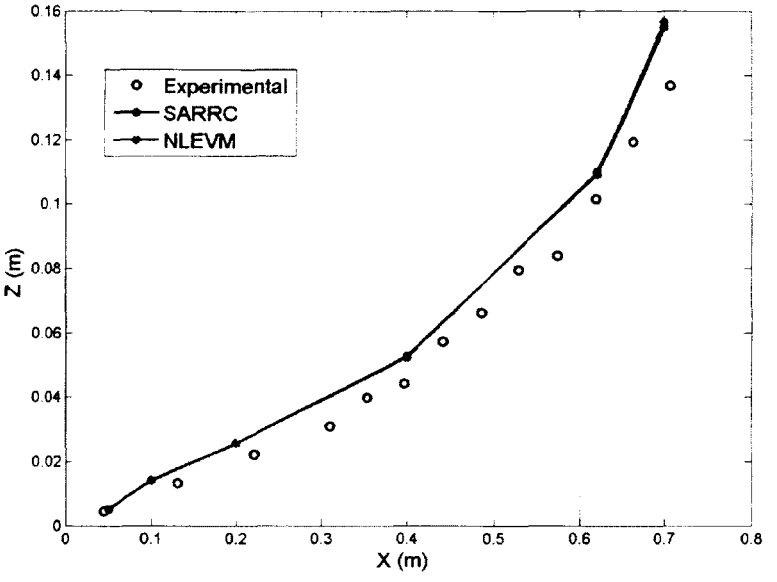

Figure 3.2. Vortex core trajectories. One-way fluid-structure interaction case.

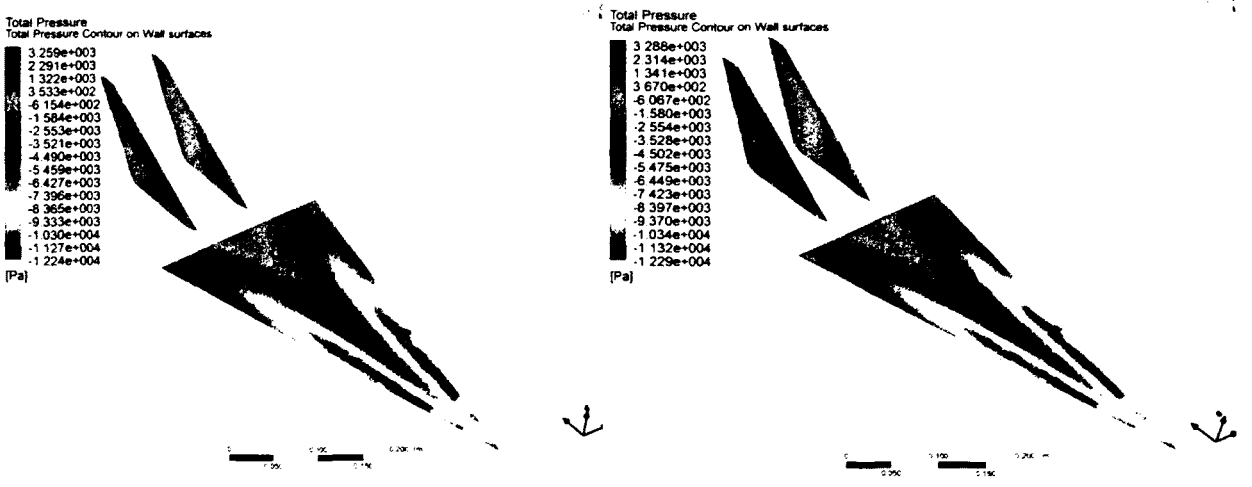

(a) SARRC (b) NLEVM

Figure 3.3. Three-dimensional view showing the total pressure contours on wing upper surface and tails. One-way fluid-structure interaction case.

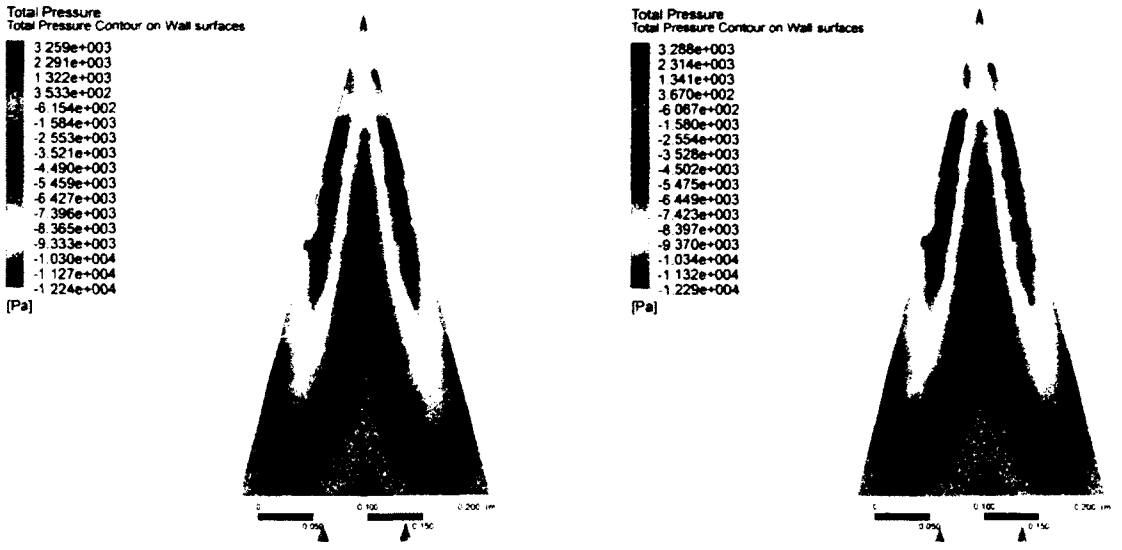

(a) SARRC

(b) NLEVM

Figure 3.4. Top view showing the total pressure contours on wing upper surface. One-way fluid-structure interaction case.

Figure 3.5 shows the snapshots of total pressure contours at four different cross flow planes using SARRC and NLEVM turbulence models. The flow structure can be viewed rather clearly. As flow moves downstream, the enlargement and weakening of the vortices can be observed. The two wing vortices impinge on the two tails. Good agreement was observed between the two turbulence models with a maximum difference of 2% in the vortex core region.

Figure 3.6 shows the pressure distribution on the upper surface of the delta wing for the two turbulence models. The locations of the effect of the two vortices on the wing upper surface can be found at the suction peaks. Both of the turbulence models show a good agreement for the surface pressure distribution.

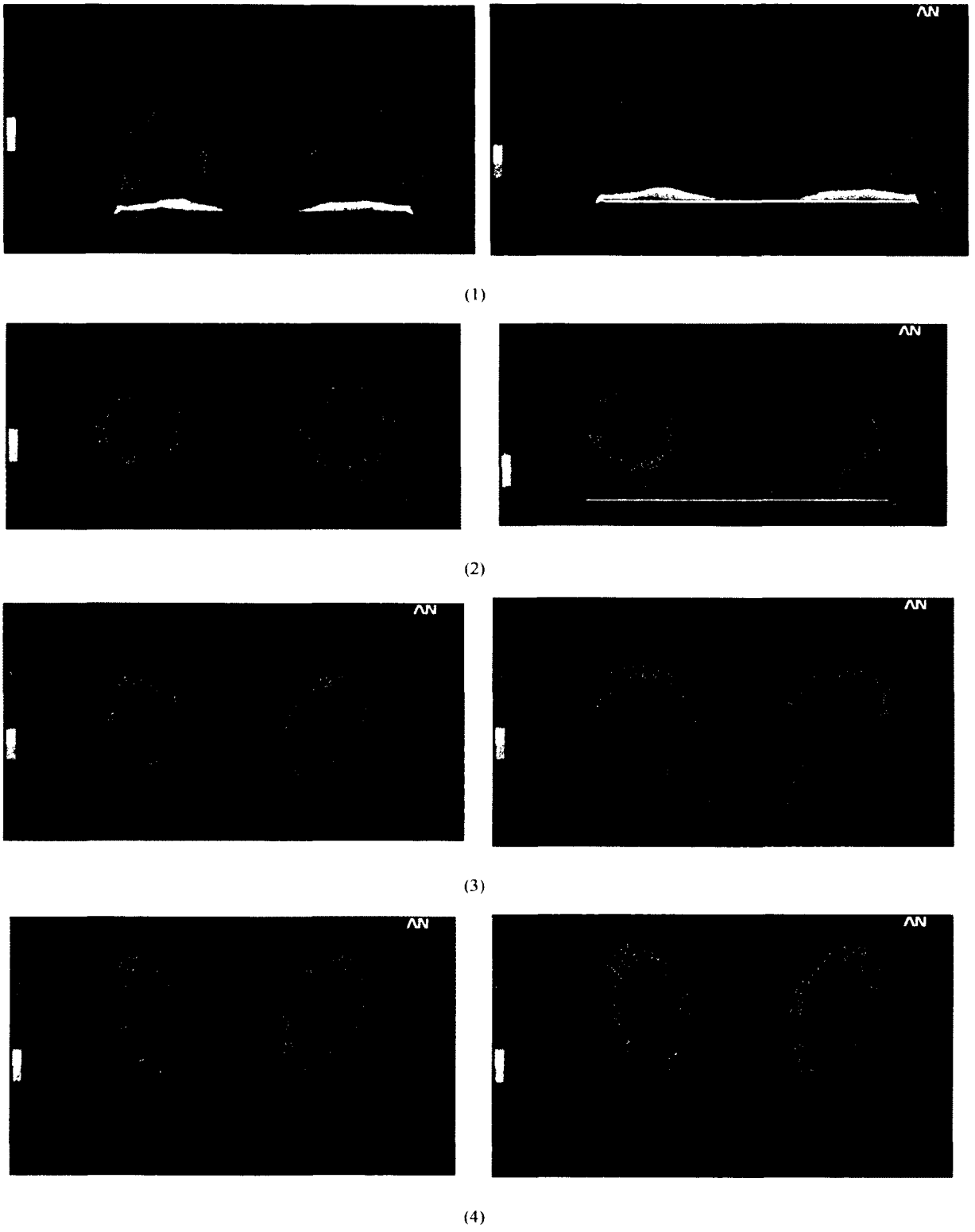

Figure 3.5. Total pressure contours on cross flow planes (1) x= 0.2 m (2) x= 0.4 m (3) x= 0.62 m (4) x= 0.7 m. One-way fluid-structure interaction case.

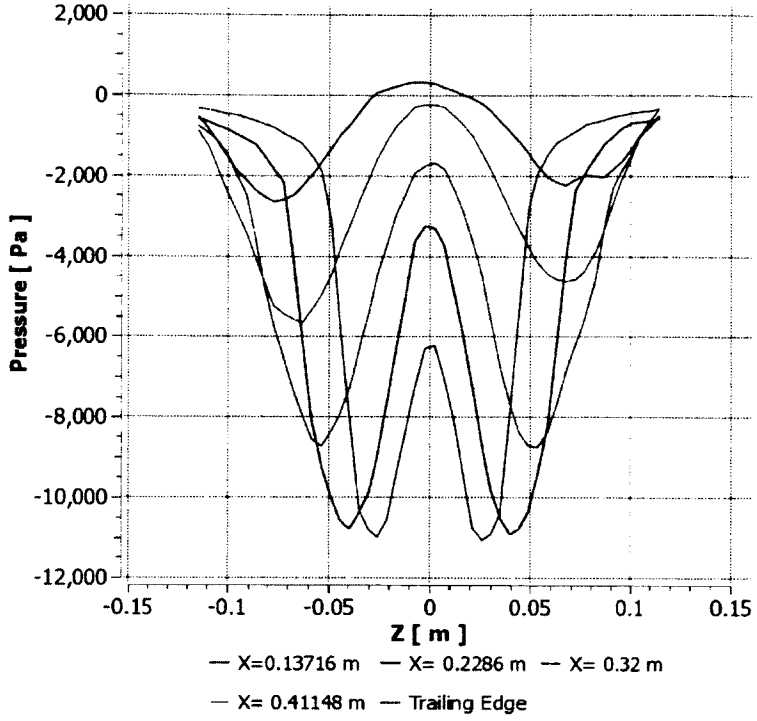

(a) SARRC

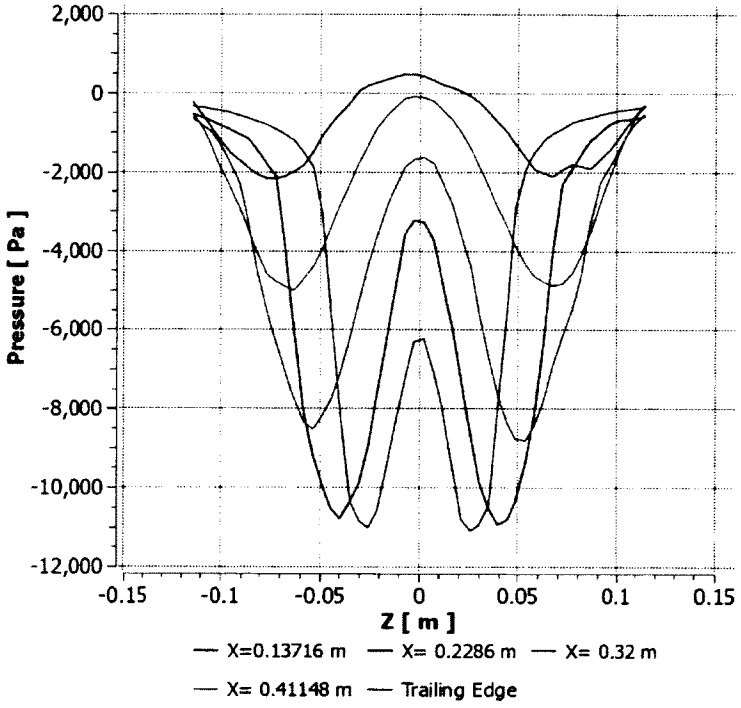

(b) NLEVM

Figure 3.6. Pressure distributions on the upper surface of the delta wing. One-way fluid-structure interaction case.

Figure 3.7 shows the stream lines across the wing. The stream lines, retraced from a line below the wing apex, enable showing the shape of the two vortices. A good agreement between the two models is observed. The formation of the two vortices can be noticed on the upper surface of the delta wing. By tracing the vortex cores, the cores started to breakdown where the stream lines bell out.

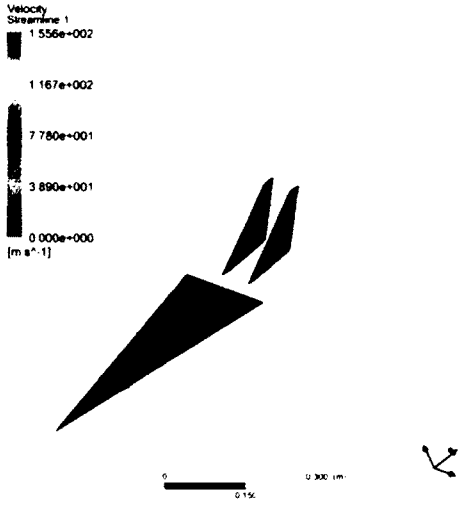

(a) SARRC

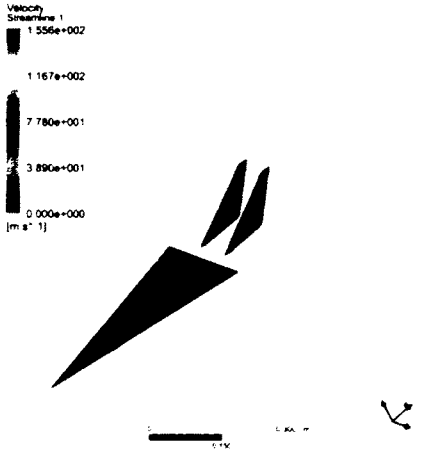

(b) NLEVM

Figure 3.7. Stream lines through the vortex core. One-way fluid-structure interaction case.

Table 3.1 shows the comparison of the RMS-computed non-dimensional pressure difference at the five specified transducer locations of the inner and outer surfaces of the right tail. The simulation results are compared with the experimental data by Washburn [26] (refer to Figure 2.1 for pressure transducers locations.) Results from both models deviate from the experimental data, with an average of 660% for NLEVM turbulence model and 535% for SARRC turbulence model. As expected, this is due to the unsteady nature of the physical flow and the movements of the tails effect on the flow, which are, of course, neglected in the steady RANS, one-way fluid-structure interaction computations. The steady one-way fluid structure interaction simulations were conducted to test if the computer code was able to predict the main flow features.

Table 3.1. One-way fluid-structure interaction case with steady-state computations. Comparison of the RMS values of non-dimensional pressure differences at five specified transducer locations of the inner and outer surfaces of the right tail.

Transducer	**1**	**2**	**3**	**4**	**5**	**Average**
Experimental	0.090	0.063	0.170	0.167	0.070	
CFD SARRC	0.462	0.004	0.124	0.386	0.717	
% Difference	413.3	94.4	27.2	130.9	2009.3	535.0
CFD NLEVM	0.446	0.160	0.156	0.379	0.924	
% Difference	395.6	154.0	8.2	126.7	2619.1	660.7

3.2 Results for steady LES, One-Way Fluid-Structure Interaction Case

A comparison between the RANS NLEVM turbulence model and LES were conducted for a steady, one way fluid-structure interaction simulation of the wing only. LES simulations require much finer grid and smaller time step. The twin-tails were not included in these simulations to reduce the large computational run time required by LES

simulation. The mesh consists of 1,131,237 elements. Due to the filtering technique used in LES, LES simulation is a transient simulation where the solution is marched in pseudo time, i.e. not physical time. The LES simulation was conducted with a time step of 10^{-3} sec and by using algebraic Wall-Modeled LES (WMLES) for subgrid-scale model. Simulations of the flow were continued up to the time when the flow was approximately statically steady. A comparison of the pressure on the wing upper surface at a distance of 0.32 m from the tip for both models is shown in Figure 3.8. A good agreement is observed between the two models with a maximum difference of 3% in the right suction peak.

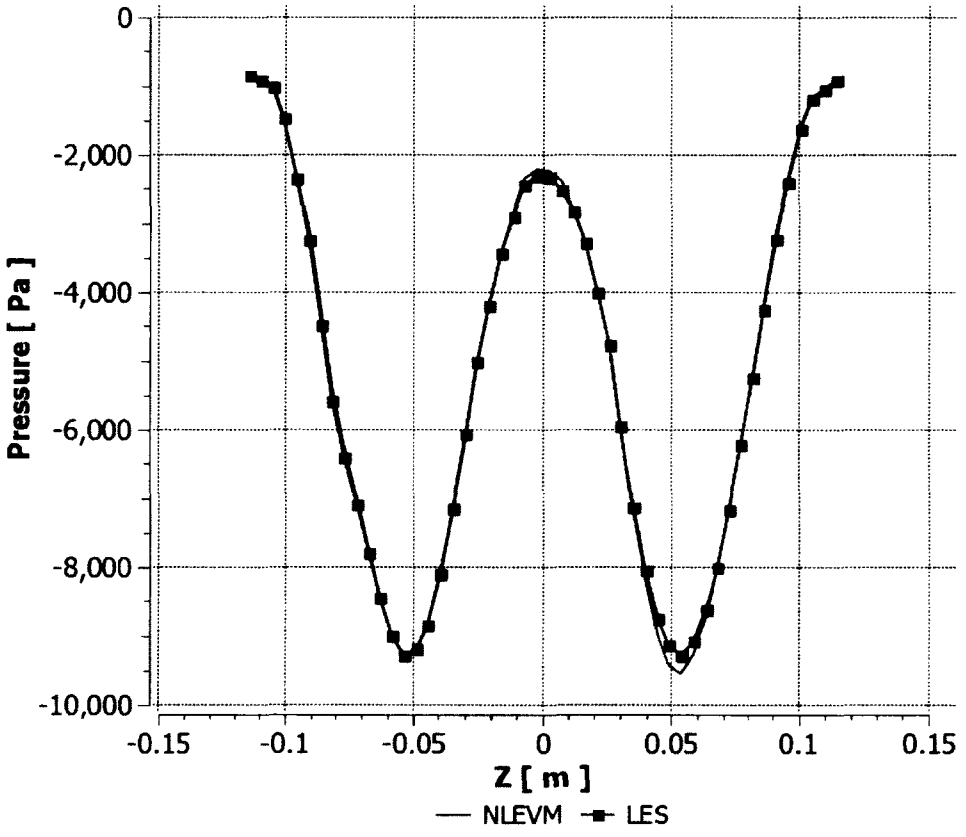

Figure 3.8. Comparison of the pressure distribution on the upper surface of the wing at a distance of 0.32 m from the wing tip for RANS NLEVM turbulence model and LES simulations. One-way fluid-structure interaction of the wing-only case.

A comparison of wall clock time per iteration and time to convergence for the two non-linear RANS turbulence models and LES simulation was conducted. The simulations for the comparisons were conducted for a steady one way fluid-structure interaction simulation of the wing-only as shown in Table 3.2. It is observed that the LES steady simulation is approximately 16 and 13 times more computationally expensive to iterate than the two RANS turbulence models SARRC and NLEVM; respectively. Also observed in Table 3.2 is that LES steady simulation is approximately 5.2 and 4.4 times more computationally expensive to converge than the two RANS turbulence models SARRC and NLEVM; respectively. Due to the high computational cost required for the LES simulations, the two-way fluid-structure interaction simulations will be conducted using RANS. Moreover, the NLEVM turbulence model simulation was approximately 1.18 times more computationally expensive to converge and to iterate than the SARRC turbulence model.

Table 3.2. One-way fluid-structure interaction wing only case. Comparison of the simulation wall clock time per iteration and physical time to converge for the two non-linear RANS turbulence models and LES.

	SARRC	NLEVM	LES
Wall clock time per iteration [sec]	37.29	44.14	576.68
Time to convergence [hr]	4.76	5.60	24.50

3.3 Results for Unsteady RANS, Two-Way Fluid-Structure Interaction Case

In two-way fluid structure interaction simulation, the fluid domain solver ANSYS Fluent and the structural domain solver ANSYS Mechanical run simultaneously every time step. Both solvers exchange data. The fluid domain solver ANSYS Fluent exports forces to the structural domain solver ANSYS Mechanical. The structural domain solver ANSYS

Mechanical exports displacement to the fluid domain solver ANSYS Fluent. Both domain solvers iterate and stop when the domain solver reaches its convergence target or the specified max number of iterations. Solver iterations within each time step are conducted and stop when the forces / displacements reach their convergence targets target or the specified max number of iterations.

The two-way fluid-structure interaction simulations have been conducted for a physical time of 0.1 sec using SARRC and NLEVM turbulence models with 10^{-3} sec time step. This time step was chosen to demonstrate the amount of fidelity that can be achieved by optimizing the available computational power. Results at 0.01 sec will be presented. Finally, the time history of the tip displacement will be presented. The present investigation is the first ever study of a tail buffet problem with a two-way fluid-structure interaction and using the two non-linear turbulence models: NLEVM, and SARRC.

3.3.1 Results at 0.01 Seconds, Two-Way Fluid-Structure Interaction Case

Figures 3.9 and 3.10 show the total pressure contours for the upper surface of the wing using SARRC and NLEVM turbulence models. The increase of the total pressure indicates the vortex breakdown. Figures 3.9 and 3.10 show the footprint of the two vortices in the region of high suction and the gradual decrease of suction as the vortices move downstream after the breakdown. The agreement between SARRC and NLEVM is very good. The two vortex breakdowns are symmetric. The vortex breakdown locations are almost the same for both turbulence models.

Figures 3.11 shows snapshots of total pressure contours at four different cross flow planes using SARRC and NLEVM turbulence models and allow the structure of the flow to be computed clearly. A gradual decrease of vortex core total pressure and

increase in the core size as the vortex moves downstream can be noticed due to the vortex breakdown. The minimum of the total pressure contour occurs at the vortex core. A significant total pressure gradient can be noticed near the tail surface at x = 0.62 m cross plane. The two wing vortices impinge on the two tails. It can be noticed that there is a little asymmetry between the left and right vortex, especially in the vortex core. This is due to the unsteady nature of the vortex breakdown, which was confirmed by the experimental data by Lee [25]. A good agreement between the two turbulence models in the relative strength of the total pressure values and the geometry of the vortex can be noticed. The maximum difference of the total pressure between the two turbulence models is 0.2% in the vortex core region.

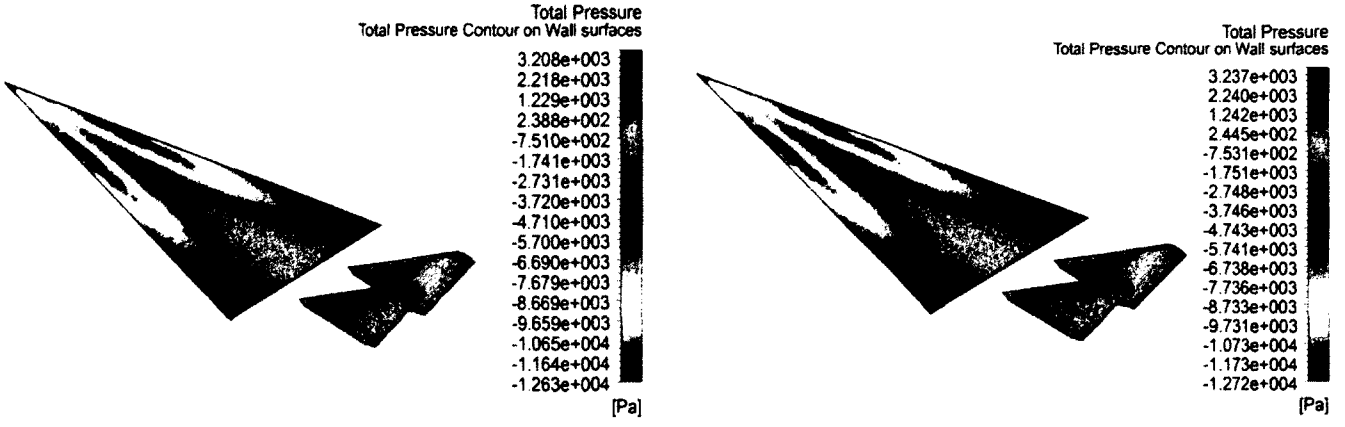

(a) SARRC (b) NLEVM

Figure 3.9. Three-dimensional view showing the total pressure contours on wing upper surface and tails. Two-way fluid-structure interaction case at 0.01 sec.

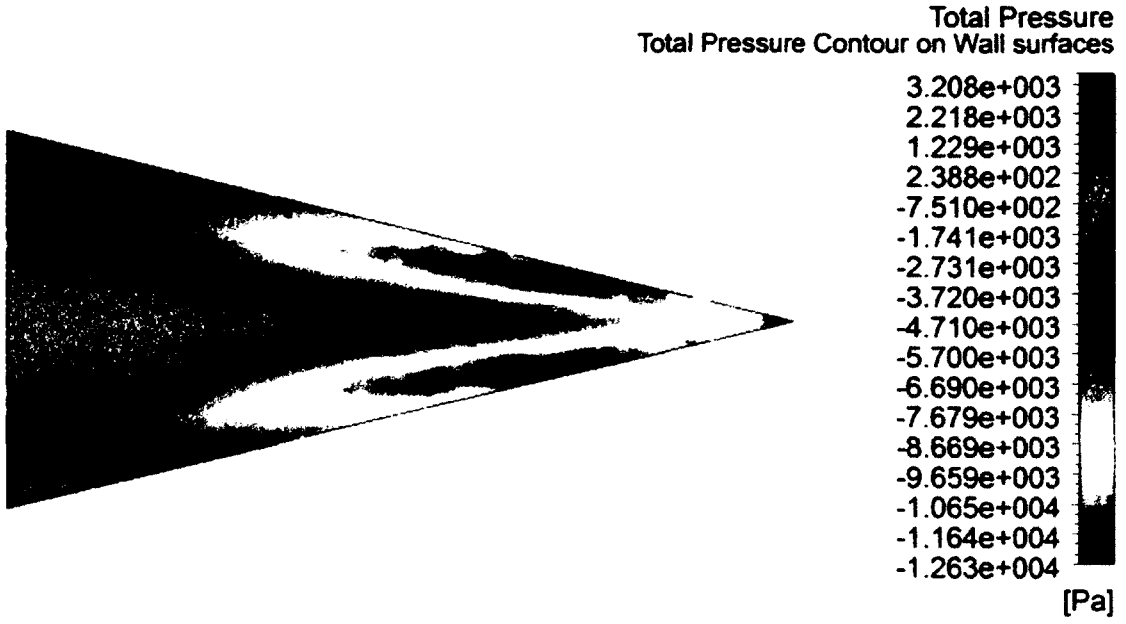

(a) SARRC

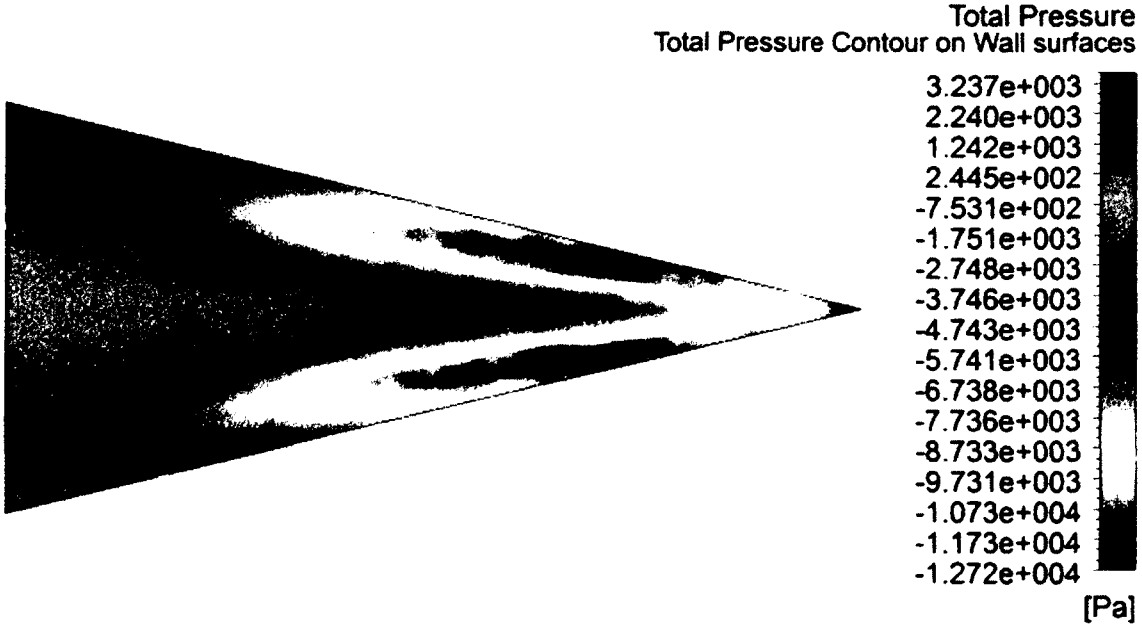

(b) NLEVM

Figure 3.10. Top view showing the total pressure contours on wing upper surface. Two-way fluid-structure interaction case at 0.01 sec.

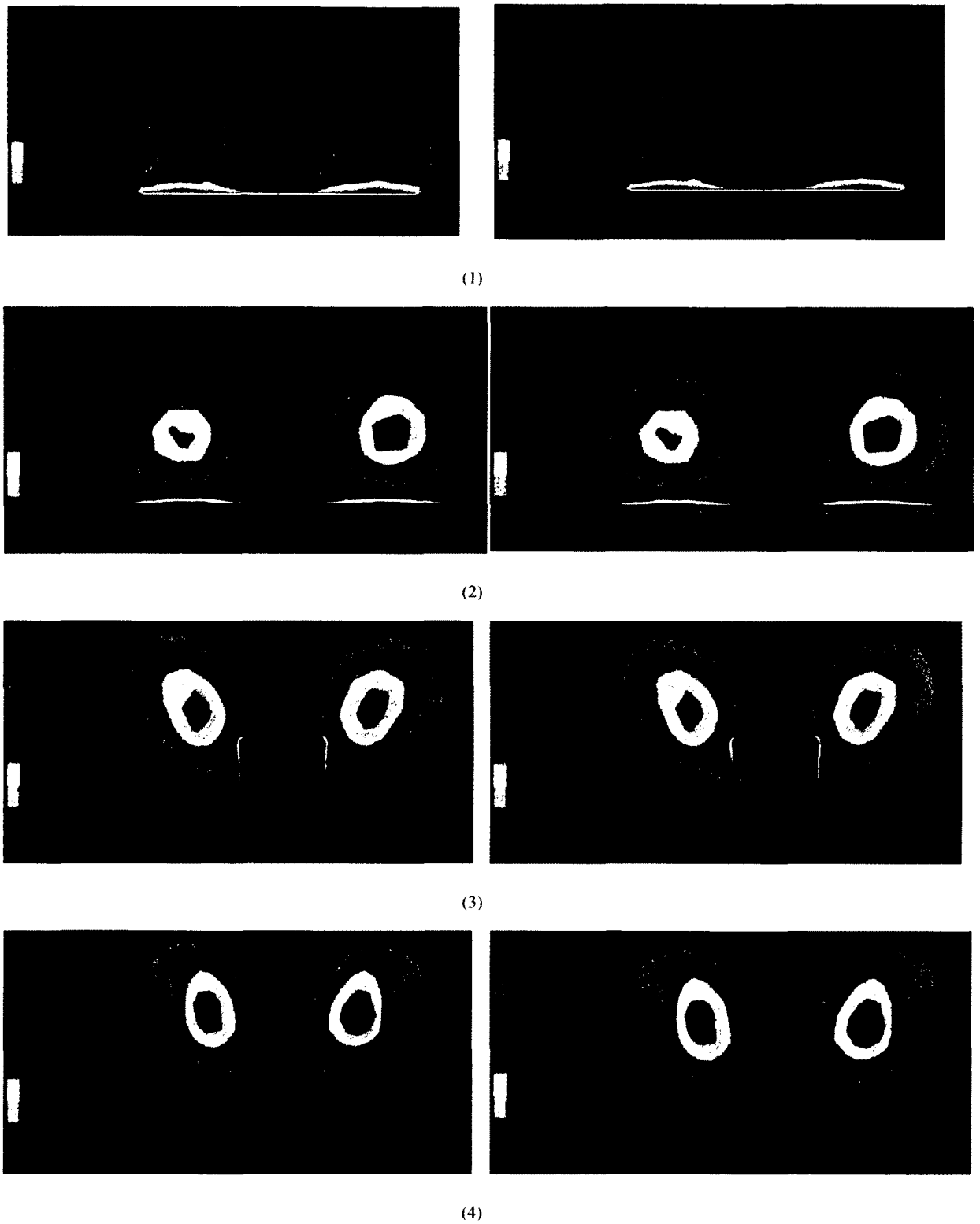

Figure 3.11. Total Pressure Contours on cross flow planes (1) x= 0.2 m (2) x= 0.4 m (3) x= 0.62 m (4) x= 0.7 m. Two-way fluid-structure interaction case at 0.01 sec.

Figure 3.12 shows the pressure distributions on the upper surface of the delta wing for the two turbulence models. The effect of the two vortices on the wing upper surface can be found in the two suction peaks. Both of the turbulence models show a good agreement for the surface pressure distribution. There is an asymmetry at the line drawn 0.13 meter from the wing apex for both of the turbulence models. Comparison of the suction peak pressure magnitudes for both one-way and two-way simulations, show that the peaks of the two-way simulations are lower at x=0.32 m and x=0.41 m than those of the one-way case. This is an indication of the weaker core and that the breakdown occurs earlier in the two-way simulations.

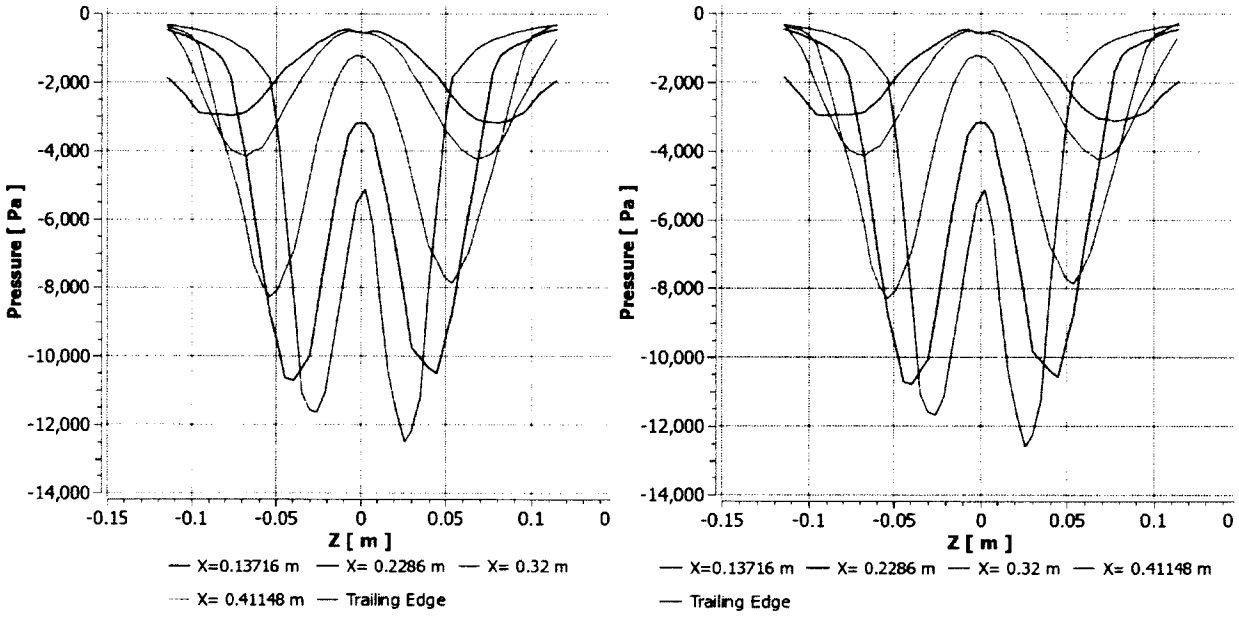

(a) SARRC (b) NLEVM

Figure 3.12. Pressure distributions on the upper surface of the delta wing. Two-way fluid-structure interaction case at 0.01 sec.

Figure 3.13 shows stream lines across the wing. The stream lines were retraced from a line below the wing apex enabling the two vortex structures to be obtained. A good agreement between the two models can be noticed. The vortex is initially stable and

intact, and then it experiences a breakdown above the surface of the wing which results in sudden enlargement of the vortex core size and a highly disturbed wake.

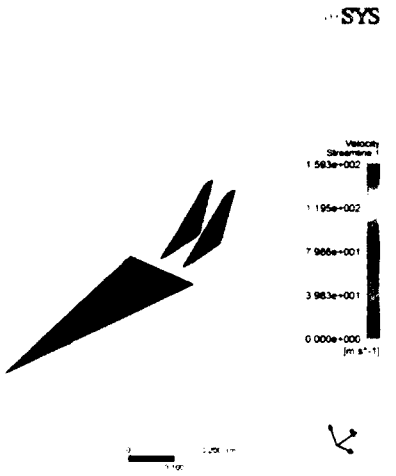

(a) SARRC

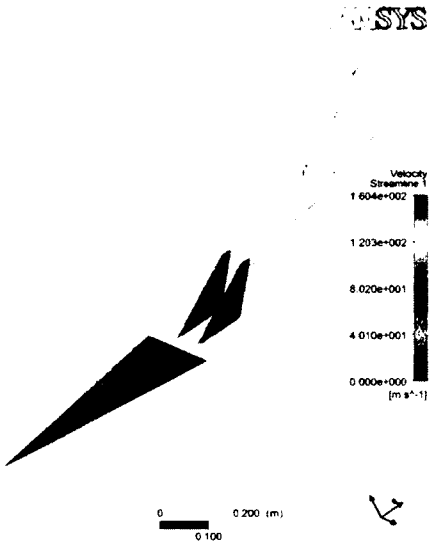

(b) NLEVM

Figure 3.13. Stream lines through the vortex core. Two-way fluid-structure interaction case at 0.01 sec.

Figures 3.14 and 3.15 show the total pressure below the vortices on the wing surface. The breakdown location could be identified from this graph at 0.15 m from apex. A good agreement between the two turbulence models can be noticed.

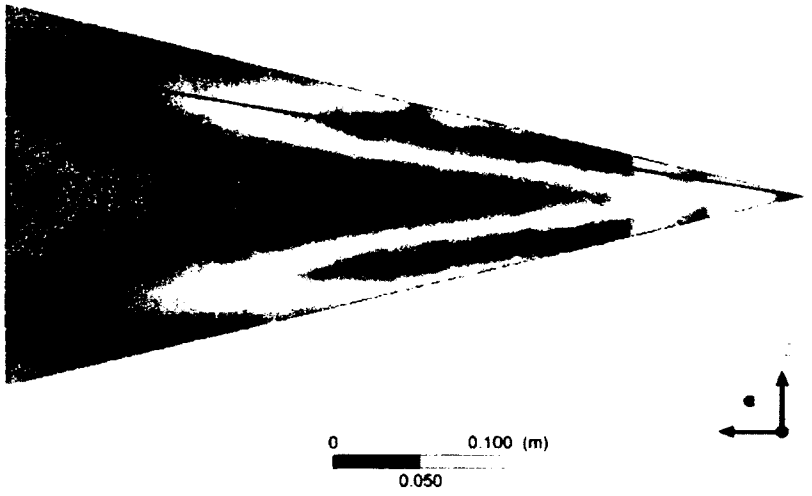

Figure 3.14. Line under vortex core on wing upper surface used to draw the total pressure.

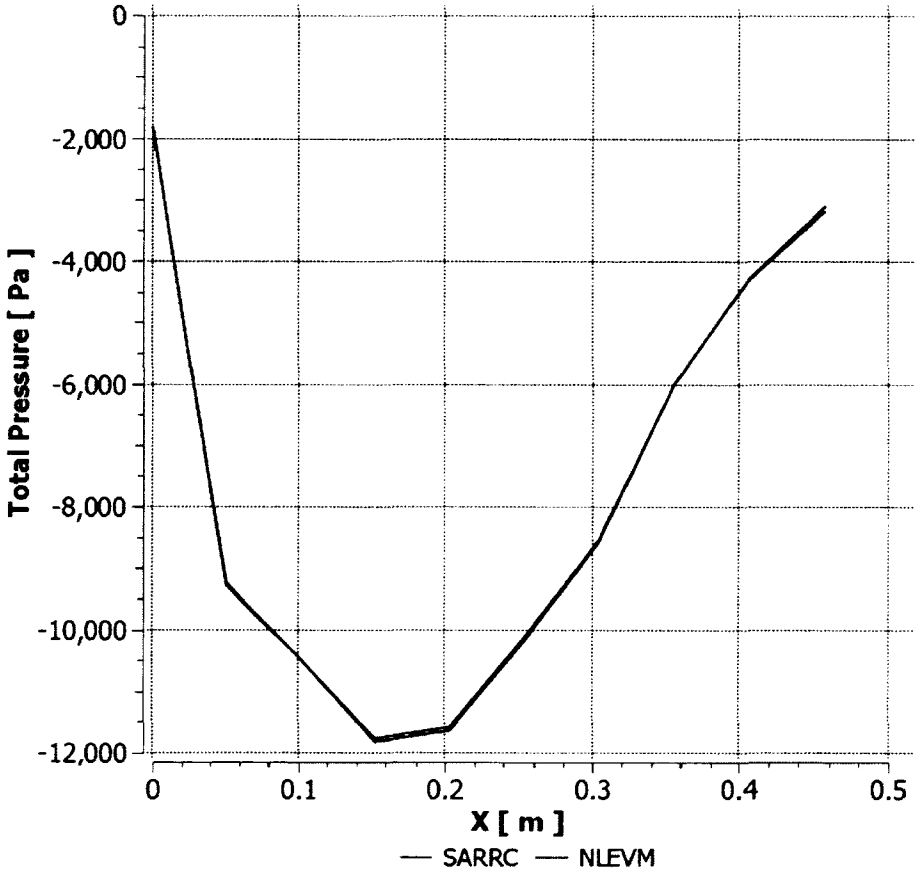

Figure 3.15. Total pressure under vortex core on wing surface. Two-way fluid-structure interaction case at 0.01 sec.

3.3.2 Time History Results, Two-Way Fluid-Structure Interaction Case

The time history of the rear tip bending displacement in lateral direction to the flow for the SARRC and NLEVM turbulence models of the right tail is shown in Figure 3.16. The amplitude and frequency of vibration is similar for both turbulence models at the beginning until 0.02 sec and both of them are close to being periodic. Afterwards they start to deviate and both show a lack of periodicity. In the beginning, the tail starts to move from rest and the applied force is due to the flow initial conditions. Later on, due to the difference between the turbulence models, the flow conditions change around the tails. The unsteady nature of the vibration of the tail tip can be noticed.

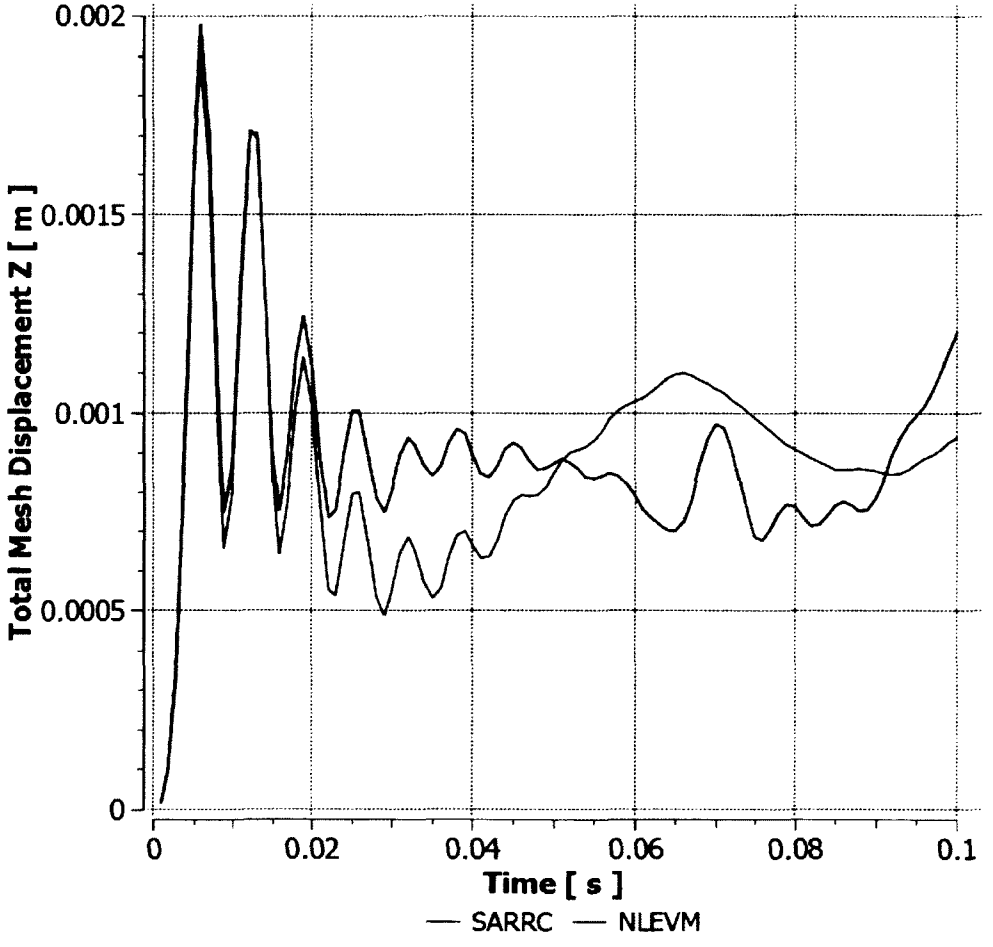

Figure 3.16. Time history of the right tail tip Z direction displacement. Two-way fluid-structure interaction case.

The time histories of the surface total pressure are used to calculate the differential pressure as the difference between the inner and the outer surface pressure values on the right tail. These values are root-mean-square (RMS) averaged. Shown in Tables 3.2 and 3.3 are the comparison with the experimental data conducted by Washburn [26] at 0.02 and 0.1 sec; respectively, of the computed RMS non-dimensional pressure difference at the five specified transducer locations of the inner and outer surfaces of the right tail, refer to Figure 2.1 for pressure transducers location. In Table 3.3, agreement between the two turbulence models is observed considering the relatively short computational time. Both SARRC & NLEVM turbulence models' computations differ from the experimental data with averages of 127% and 124%, respectively. Overall the NLEVM turbulence model gave a slightly enhanced agreement than SARRC turbulence model. The large error percentages in Table 3.3 are due to the short-than-ideal run times of these two-way fluid-structure interaction simulations (0.02 sec). A better error percentage should be expected by running the simulations for a longer time.

Table 3.3. Two-way fluid-structure interaction cases for a total simulation time of 0.02 sec. Comparison of the computed RMS non-dimensional pressure difference at the five specified transducer Locations of the inner and outer surfaces of the right tail.

Transducer Location	1	2	3	4	5	Average
Experimental	0.090	0.063	0.170	0.167	0.070	
CFD SARRC	0.141	0.074	0.199	0.279	0.196	
% Difference	57.3	18.7	16.5	67.2	478.4	127.6
CFD NLEVM	0.141	0.078	0.193	0.275	0.192	
% Difference	57.5	24.3	13.1	64.4	464.7	124.8

Additional analyses were conducted by running the simulations for a longer time. Table 3.4 shows the result for the 0.1 sec simulation. Better results occurred especially for pressure transducer 5 when compared at 0.02 sec simulations. The average error dropped to 49% for NLEVM turbulence model and 52.6% for SARRC turbulence model. Some points were much closer to the experimental data, within 3.7% for NLEVM turbulence model and 10.9% for SARRC turbulence model. Overall, the NLEVM turbulence model gave better agreement with experimental data than SARRC turbulence model as expected. The enhancement of the average difference of the RMS total pressure simulation data with experimental data can be noticed from Table 3.3 to Table 3.4. This is because the simulation was run for a longer time and two-way fluid-structure interaction was considered. Better RMS total pressure values should be expected if the simulations were run for even longer time, such as 0.5 sec.

Table 3.4. Two-way fluid-structure interaction cases for a total simulation time of 0.1 sec. Comparison of the computed RMS non-dimensional pressure difference at the five specified transducer Locations of the inner and outer surfaces of the right tail.

Transducer Location	1	2	3	4	5	Average
Experimental	0.090	0.063	0.170	0.167	0.070	
CFD SARRC	0.013	0.052	0.189	0.258	0.00097	
% Difference	84.7	15.9	10.9	54.6	97.1	52.6
CFD NLEVM	0.011	0.070	0.164	0.244	0.00069	
% Difference	87.1	11.8	3.7	46.0	97.9	49.3

SARRC turbulence model is based on the one-equation turbulence model the Spalart-Allmaras. Moreover the Spalart-Allmaras model coefficient was derived from experimental data for types of flow which is different than the vortical flow of this

problem. A one-equation turbulence model provides one independent transport equation for the un-damped eddy viscosity. The NLEVM turbulence model is based on the two equation turbulence model, Wilcox $k-\omega$. The two-equation turbulence model provides two independent transport equations for the dissipation and the turbulent kinetic energy. With the specification of these two variables, two-equation models can capture more flow characteristics when compared to the one-equation turbulence models. On the other hand, NLEVM turbulence model is computationally more expensive than SARRC turbulence model as it involves the solutions of two transport equation compared to one equation for SARRC turbulence model. A comparison of the simulation wall clock time per iteration and physical time to converge for the two non-linear RANS turbulence models were presented in Table 3.2.

Table 3.5 shows a comparison between one and two-way fluid-structure interaction simulation cases by using the two non-linear eddy viscosity turbulence models SARRC and NLEVM. This comparison of the results gave an indication that the time averaged steady-state, one-way simulations are not able to predict the RMS values of the pressure on the tails. For two-way fluid-structure simulations, NLEVM turbulence model gives better pressure results because of the smaller production of the turbulence in the vortex core. This leads to less vorticity diffusion, resulting in a stronger vortex. A stronger vortex indicates high velocity and low pressure within the vortex core.

Table 3.6 lists the average error between the computed RMS pressure values for two-way fluid-structure interaction simulations by using linear eddy viscosity turbulence models by other researchers and the current two-way fluid-structure interaction simulations. In Table 3.5, simulation results were compared with the experimental data.

The results by Sheta [40] and Guillaume [41] were supported by a large research team for much longer periods. In the present study, considering the available computational resources, very good results were obtained by for a simplified geometry of the F/A-18.

Table 3.5. Comparison of the numerically computed RMS non-dimensional pressure difference average error on the tail surface for one and two-way fluid structure interaction cases by using SARRC and NLEVM turbulence models.

Simulation case	Turbulence model	Average error between the computed RMS pressure values and experimental data
One Way	SARRC	535.0%
	NLEVM	660.7%
Two Way	SARRC	52.6%
	NLEVM	49.3%

Table 3.6. Two-way fluid-structure interaction simulations of a F/A-18 tail buffet. Comparison of the numerically computed RMS non-dimensional pressure differences, average error on the tail surface by different researchers.

Researcher	Average error between the computed RMS pressure values and experimental data	F/A-18 model
Massey [38]	63%	Simplified Geometry
Leviniski [1]	40%	Simplified Geometry
Sheta [40]	37%	Full-scale
Guillaume [41]	32%	Full-scale
Present study SARRC	52.6%	Simplified Geometry
Present study NLEVM	49.3%	Simplified Geometry

CHAPTER 4

CONCLUSIONS AND RECOMMENDATIONS

4.1 Conclusions

A computational model for the prediction of the unsteady aeroelastic behavior of a flexible tail under buffet-induced loads has been investigated. The URANS equations with two non-linear turbulence models have been used to model the flow and finite element analysis by using shell elements to model the structural dynamics of the tail. The fluid solver ANSYS Fluent was used in the fluid domain simulations. The two turbulence models are the modified Spalart-Allmaras model (SARRC) with a rotation/curvature based production and curvature treatment, and the Non-linear Eddy Viscosity Model (NLEVM) turbulence model. The NLEVM turbulence model is based on the standard Wilcox k–ω model and uses the formulation of an explicit algebraic Reynolds stress model proposed by Wallin and Johansson to model the Reynolds stresses. Both SARRC and NLEVM turbulence models are in ANSYS software.
The structural solver ANSYS Mechanical was used in the tail simulation. The vertical tail of the F/A-18 aircraft is modeled using SOLID186 elements.

The experimental data used for comparison are by Washburn [26]. Washburn obtained data on a simplified geometry: a Mach 0.3 flow and a Reynolds number of 3.7×10^6 past a 76-deg delta wing pitched to 30-deg angle of attack. Two vertical tails were placed downstream of the delta wing.

The present work is the first ever study of a tail buffet problem with a two-way fluid-structure interaction and using the two advanced non-linear turbulence models: NLEVM and SARRC. The steady-state, time-averaged, one-way fluid-structure

interaction case indicates that both NLEVM and SARRC turbulence models results do not compare well with the experimental data. These results were expected for the steady-state, one-way simulations, because it involved no force and displacement transfer from the structure to the fluid solver. The steady one-way fluid structure interaction simulations were conducted to confirm that the simulation code is able to predict the main features of the flow. A comparison between LES and steady RANS simulation was also conducted for the wing only. Both LES and steady RANS models were able to predict the two vortices and their effect on the wing surface. Due to the high computational cost required for the LES simulations, the two-way fluid-structure interaction simulations were conducted for the two RANS turbulence models SARRC and NLEVM only.

For the unsteady two-way fluid-structure interaction case, both models result in more favorable agreement with the experimental data by optimizing the available computational resources, particularly when compared to prior simulations by other researchers. Results from the NLEVM turbulence model produce improved pressure values on the tail as compared to the results from the SARRC turbulence model.

Therefore, it is concluded that the buffet problem should be modeled and simulated as a two-way fluid-structure interaction. Also, NLEVM turbulence model is recommended in predicting vortical flow characteristics over a delta wing. This is particularly necessary to predict the pressure values not only over the aircraft's surfaces but also the tails since they experience the wake of the vortices.

4.2 Recommendations

Based on the current simulation results, the following recommendations should be considered in future research:

1. The simulations should be conducted by using a smaller time step.
2. More comparisons with different experimental data should be conducted at different Reynolds numbers to validate these models.
3. By optimizing the available computational resources for the pre-compiled software executable file used, the simulation run time was chosen as 0.1 sec. Running the simulations longer would be recommended. Other researchers recommended 0.5 sec to capture the main frequencies of the flow.
4. For higher-fidelity results, it is recommended to use DES based on SARRC and NLEVM for the two-way fluid-structure interaction simulations.

REFERENCES

[1] Levinski, O., "Vertical tail dynamic response in vortex breakdown flow," DSTO-RR-0256 Research Report, Air Vehicles Division, Platforms Sciences Laboratory, Department of Defense, Australian Government, June 2003.

[2] Robert, A., Canfield, Morgenstern, S. D. and Kunz, D., L., "Alleviation of buffet-induced vibration using piezoelectric actuators," *Computers and Structures*, Vol. 86, 2008, pp. 281–291.

[3] Hanagud, S., Bayon de Noyer, M., Luo, H., Henderson, D. and Nagaraja, K. S., "Tail buffet alleviation of high-performance twin-tail aircraft using piezo-stack actuators," *AIAA Journal*, Vol. 40, No.4(4), 2002.

[4] Technical Report by the Accident Investigation Sub-committee on the Accident to the Airplane G. Aazk at Meophan, Kent, on 21st July, 1930, R. & M. No. 1360, British A.R.C., January 1931.

[5] Hanagud, S., "F-15 Tail buffet alleviation: a smart structure approach, Final Report," Project number: F33615-96-C-3204, Georgia Institute of Technology, 1998.

[6] Moses, R. W. and Pototzky, A. S., "Controlling Buffet Loads by Rudder and Piezo-Actuation," Forum on Aeroelasticity and Structural Dynamics, IF-086, 2005.

[7] Wickramasinghe, V. K., "Experimental Evaluation of a Full-Scale Advanced Hybrid Buffet Suppression System for the F/A-18 Vertical Tail," 47th AIAA/ASME/ASCE/AHS/ASC Structures, Structural Dynamics, and Materials Conference, 1 - 4, Newport, Rhode Island, May 2006.

[8] United States Navy website: www.navy.mil.

[9] Alex Betyukov collection: www.airliners.net.

[10] Pakistan Defense website: www.defense.pk.

[11] Cunningham, A. and Buzz M., "Buffet and LCO on military aircraft— the aeroelastician's nightmares," Technical Report, Fort Worth, TX: Lockheed Martin Aeronautics Company; 2003.

[12] Moses, R. W., "Active Vertical Tail Buffeting Alleviation On a Twin Tail Fighter Configuration In a Wind Tunnel," CEAS International Forum on Aeroelasticity and Structural Dynamics, Rome, Italy, June 1997.

[13] Lee, B. H. K., Brown, D., Zdela, M. and Poirel, D., "Wind tunnel investigation and flight test of tail buffet on the CF-18 aircraft," AGARD CP-483, Aircraft Dynamic Loads due to Flow Separation, 1990.

[14] Lee, B. H. K. and Valerio, N. R., "Vortical Flow structure near the F/A-18 LEX at high incidence," *Journal of Aircraft*, Vol. 31(5), 1994.

[15] Thompson, D. H., "Effect of the Leading Edge Extension (LEX) Fence on the Vortex Structure over the F/A-18," Aeronautical and Maritime Research Laboratory, DSTOTP-0489, 1997.

[16] Inan, S., "AETE PD98/26 F/A-18 Flight Test Dynamic Response Results," Australian Department of Defence, DSTO, Aeronautical and Maritime Research Laboratory, Technical Report, DSTO-TR-1252, 2002.

[17] Houghton, E. L. and Carpenter P., *Aerodynamics for Engineering Students*, Butterworth Heinemann, fifth edition, 2003.

[18] Hoeijmakers, H. W. M., "Modeling and numerical simulation of vortex flow in aerodynamics," In AGARD Conference Proceedings "Vortex Flow Aerodynamics", AGARD-CP-494, July 1991.

[19] Polhamus, E. C., "Vortex Lift Research: Early Contributions and Some Current Challenges," NASA CP-2416, Vol. 1, July 1986.

[20] Anderson, J. D., *Fundamentals of Aerodynamics*, McGraw-Hill, second edition, 1991.

[21] Luckring, J. M., "A Survey of Factors Affecting Blunt Leading-Edge Separation for Swept and Semi-Slender Wings," AIAA-2010-4820, Jun 2010.

[22] Sellers, W. L. III, Meyers, J. F. and Hepher, T. E., "LDV surveys over a fighter model at moderate to high angles of attack," SAE Paper 88-1448, Aerospace Technology Conference and Exposition, Anaheim, California, October 1988.

[23] Erickson, G. E., "Wind Tunnel Investigation of Vortex Flows on F/A-18 at Subsonic Through Transonic Speeds," NASA TP 3111, December 1991.

[24] Wentz, Jr., W. R., "Vortex-fin interaction on a fighter aircraft, AIAA 7th Lighter-than-Air Technology Conference," AIAA 87-2474, Monterey, California, August 1987.

[25] Lee, B. H. K., Brown, D., Zgela M. and Poirel D., "Wind tunnel investigation and flight tests of tail buffet on the CF-18 aircraft," AGARD CP-483, Aircraft Dynamic Loads due to Flow Separation. 1990.

[26] Washburn, A. E., Jenkins, L. N. and Ferman, M. A., "Experimental Investigation of Vortex-Fin Interaction," AIAA Paper 93-0050, Reno, NV, 1993.

[27] Moss, S. W., Cole, S. R. and Doggett, Jr., R. V., "Some subsonic and transonic buffet characteristics of the twin-vertical-tails of a fighter airplane configuration," AIAA 91-1049-CP, AIAA/ASME/ASCE 32nd Structures, Structural Dynamics, and Materials Conference, 1991.

[28] Meyn, L. A., Lanser, W. R. and James, K. D., "Full-scale high angle-of-attack tests of an F/A-18," AIAA 92-2676, 10th AIAA Applied Aerodynamics Conference, Palo Alto, California, June 1992.

[29] Meyn, L. A. and James, K. D., "Full Scale Wind Tunnel Studies of F/A-18 Tail Buffet, AIAA Applied Aerodynamics Conference," AIAA 93-3519, Monterey, CA, August 1993.

[30] Meyn, L. A. and James, K. D., "Full scale wind tunnel studies of F/A-18 tail buffet," *Journal of Aircraft*, Vol. 33(3), 1996.

[31] Meyn, L. A. and James, K. D., "Integrated tail buffet loads on the F/A-18," AIAA 94-1801, 12th AIAA Applied Aerodynamics Conference, Colorado Springs, Colorado, June 1994.

[32] Meyn, L. A., James, K. D., and Geenen, R. J., "Correlation of F/A-18 Tail Buffet Results," High-Alpha Projects & Technology Conference, NASA Dryden Flight Research Center, July 1994.

[33] Moses, R. W. and Pendleton, E., "A comparison of pressure measurements between a full-scale and a 1/6-Scale F/A-18 twin tail during buffet," NASA TM-110282, 1996.

[34] Fisher D. F., Del Frate J. H. and Richwine D. M., "In-Flight Flow visualization characteristics of the NASA F-18 High Alpha Research Vehicle at high angles of attack". NASA TM-4193, 1990.

[35] Kandil, O. A., Kandil, H. A., and Massey, S. J., "Simulation of Tail Buffet Using Delta Wing-Vertical Tail Configuration," AIAA-93-3688-CP, AIAA Atmospheric Flight Mechanics Conference, Monterey, CA, 1993.

[36] Kandil, O. A., Sheta, E. F., and Massey, S. J., "Twin Tail/Delta Wing Configuration Buffet due to Unsteady Vortex Breakdown Flow," AIAA-96-2517-CP, 1996.

[37] Sheta, E. F., "Computational investigation and validation of twin-tail buffet response including dynamics and control," Ph.D. dissertation, Old Dominion University, 1998.

[38] Massey, S. J., "Development of a coupled fluid/structure aeroelastic solver with applications to vortex breakdown induced twin tail buffeting," Ph.D. dissertation, Old Dominion University, 1997.

[39] Findlay, D. B., "A Numerical Study of Aircraft Empennage Buffet," Ph.D. Thesis, Georgia Institute of Technology, June 1999.

[40] Sheta, E. F., "Buffet alleviation of F/A-18 aircraft using LEX fences," AIAA-2003-1888, 44th AIAA/ASME/ASCE/AHS Structures, Structural Dynamics, and Materials Conference, Norfolk, Virginia, April 2003.

[41] Guillaume, M., Gehri A. and Stephani P., "Fluid structure interaction simulation on the F/A-18 vertical tail," AIAA 2010-4613 paper, 40th AIAA Fluid Dynamics Conference and Exhibit, Chicago, IL, June 2010.

[42] Cummings, R. M., Forsythe, J. R., Morton, S. A. and Squires K. D., "Computational challenges in high angle of attack flow prediction," Progress in Aerospace Sciences, Vol. 39(5) , July 2003, pp.369–384.

[43] Brandsma, F. J., Kok, J. C., Dol, H. S. and Elsenaar, A., "Leading edge vortex flow computations and comparison with DNW-HST wind tunnel data," RTO / AVT Vortex Flow Symposium, Loen, Norway, 2001.

[44] Spalart, P. R., Jou, W. H., Streles, M. and Allmaras, S. R., "Comments on feasibility of LES for wings and on a hybrid RANS / LES approach," Proceedings of the first AFSOR International Conference on DNS/LES, Greyden Press, Columbus, OH, August 4-8 1997.

[45] Visbal, M. R. and Gordnier, R. E., "On the structure of the shear layer emanating from a swept leading edge at angle of attack," AIAA 2003-4016, June 2003.

[46] Schiavetta, L. A., "Evaluation of URANS and DES Predictions of Vortical Flow over Slender Delta Wings," Ph.D. Thesis, University of Glasgow, Glasgow, U.K., 2007.

[47] Gordnier, R. E., "Computational study of a turbulent delta wing flowfield using two-equation turbulence models," AIAA 96-2076 paper, 27th AIAA Fluid Dynamics Conference, June 1996.

[48] Wallin, S. and Johansson, A., "An explicit algebraic Reynolds stress model for incompressible and compressible turbulent flows," *Journal of Fluid Mechanics*, Vol. 403, January 2000.

[49] Hellsten, A., "New advanced k−w turbulence model for high-lift aerodynamics," AIAA Paper 2004-1120, Reno, Nevada, 2004.

[50] Wilcox, D. C., *Turbulence Modelling for CFD*, DCW Industries Inc, 1993.

[51] Wilcox, D. C., "Reassessment of the scale determining equation for advanced turbulence model," *AIAA Journal*, Vol. 26(11), November 1988.

[52] Mellor, G. L. and Herring, H. J., "A Survey of the Mean Turbulent Field Closure Models," AIAA J., 11, 1973.

[53] Rumsey, C. L., Gatski, T. B. and Morrison, J. H., "Turbulence Model Predictions of Extra-Strain Rate Effects in Strongly-Curved Flows," AIAA 99-0157, 37th Aerospace Sciences Meeting and Exhibit, Reno, NV, January 11-14, 1999.

[54] Menter, F. R., "Improved Two-Equation k-w Turbulence Models for Aerodynamic Flows," NASA TM 103975, Oct. 1992. 2000.

[55] Dol, H. S., Kok, J. C. and Oskam, B., "Turbulence modelling for leading edge vortex flows," 40th AIAA Aerospace Sciences Meeting and Exhibit, AIAA 2002-0843, January 2002.

[56] Soemarwoto, B. I. and Boelens, O. J., "Simulation of vortical flow over a slender delta wing experiencing vortex breakdown," 21st AIAA Applied Aerodynamics Conference, AIAA 2003-4215, June 2003.

[57] Schiavetta, L. A. and Badcock, K. J., "Comparison of DES and URANS for Unsteady Vortical Flows over Delta Wings," AIAA 2007-1085, January 2007.

[58] Spalart, P. R. and Allmaras, S. R., "A one equation turbulence model for aerodynamic flows," 30th AIAA Aerospace Science Meeting and Exhibit, AIAA Paper 1992-0439, January 1992.

[59] Dacles-Mariani, J., Zilliac, G. G., Chow, J. S. and Bradshaw, P., "Numerical/Experimental Study of a Wingtip Vortex in the near field," *AIAA Journal*, Vol. 33(9), 1995.

[60] Dacles-Mariani, J., Kwak, D. and Zilliac, G. G., "On Numerical Errors and Turbulence Modeling in Tip Vortex Flow Prediction," *International Journal for Numerical Methods in Fluids*, Vol. 30, 1999.

[61] Spalart, P. R. and Shur, M. L., "On the Sensitization of Turbulence Models to Rotation and Curvature," Aerospace Sci. Tech. 1(5), 1997.

[62] Shur, M. L., Strelets, M. K., Travin, A. K. and Spalart, P. R., "Turbulence Modeling in Rotating and Curved Channels: Assessing the Spalart-Shur Correction," *AIAA Journal*, Vol. 38(5). 2000.

[63] Morton, S. A., Forsythe, J., Mitchell, A. M. and Hajek, D., "Detached eddy simulation and Reynolds averaged Navier-Stokes simulations of delta wing vortical flow fields," *Journal of Fluids Engineering*, Vol. 124, December 2002.

[64] Morton, S. A, Forsythe, J., Mitchell, A. M. and Hajek, D., "DES and RANS simulations of delta wing vortical flows," 40th AIAA Aerospace Sciences Meeting and Exhibit, AIAA 2002-0587, January 2002.

[65] Pope, S. B., *Turbulent Flows*, Cambridge University Press, 2000.

[66] ANSYS Fluent Theory Guide, ANSYS, Inc. November 2011.

[67] ANSYS Fluent 14 Documentation, November 2011.

[68] Hirsh, C., "Numerical Computation of Internal and External Flow," Wiley-Interscience, Series in Numerical Methods in Engineering, Vol. 1-2, 1989.

[69] Ferziger, J. H. and Peric, M., *Computational Methods for Fluid Dynamics*, Springer 1997.

[70] Demirdzic, I. A. and Peric, M., "Finite Volume Method for Prediction of Fluid Flow in Arbitrarily Shaped Domains With Moving Boundaries," *International Journal for Numerical Methods in Fluids*, Vol. 10, 1990.

[71] ANSYS Mechanical APDL Theory Reference, ANSYS, Inc., November 2011.

[72] System Coupling User's Guide, ANSYS, Inc., November 2011.

VITA

Ahmed Mohamed Nagib Mohamed Elmetwaly Elmekawy

Education

- **Ph.D. Candidate in Mechanical and Aerospace Engineering**
  Old Dominion University, Norfolk, VA, USA, May 2014.
  Ph.D. Dissertation: Fluid-Structure Interaction Modeling of a F/A-18 Twin-Tail Buffet Using Non-Linear Eddy Viscosity Models.
  GPA: 3.74 /4.0
- **Master of Science in Mechanical Engineering**
  Alexandria University, Alexandria, Egypt, August 2009.
  Master's Thesis: Effect of Magnetic Bearings on Rotor Dynamics.
  GPA: 3.72 /4.0
- **Bachelor of Science in Mechanical Engineering**
  Alexandria University, Alexandria, Egypt, May 2006.
  B.Sc Project: Design and manufacturing of a desalination and air conditioning unit.
  GPA: 3.8/4.0

Work Experience

- **Staff Research and Development Mechanical Engineer** (2012 - Present)
  Flexible Steel Lacing Company (Flexco), Downers Grove, IL 60532
- **Research & Teaching Assistant** (2009 - 2012)
  Aerospace Engineering, Old Dominion University, Norfolk, VA, USA
- **Research & Teaching Assistant** (2006 - 2009)
  Mechanical Engineering, Alexandria University, Alexandria, Egypt.

Activities and Honors

- **Ranked 4th of 535 student in Mechanical Engineering Department** (2006)
  Alexandria University, Alexandria, Egypt
- **Undergraduate 5 year Scholarship** (2001- 2006)
  Alexandria University, Alexandria, Egypt
- **Master Assistantship** (2006 - 2009)
  Alexandria University, Alexandria, Egypt
- **Ph.D. Assistantship** (2009 - 2012)
  Old Dominion University, Norfolk, VA, USA
- **President of the Egyptian Student Association** (2012)
  Old Dominion University, Norfolk, VA, USA
- **Vice President of the Egyptian Student Association** (2011)
  Old Dominion University, Norfolk, VA, USA